

# Simultaneous measurements of scalar and velocity field evolution in turbulent crossflowing jets

By L. K. SU<sup>1</sup> AND M. G. MUNGAL<sup>2</sup>

<sup>1</sup>Department of Mechanical Engineering, The Johns Hopkins University, Baltimore, MD 21218-2681, USA

<sup>2</sup>Thermosciences Division, Mechanical Engineering Department, Stanford University, Stanford, CA 94305-3032, USA

(Received 23 May 2003 and in revised form 27 February 2004)

Simultaneous planar laser-induced fluorescence (PLIF) and particle image velocimetry (PIV) yield measurements of two-dimensional jet fluid concentration and velocity fields in turbulent crossflowing jets. The jet-to-crossflow velocity ratio is  $r = 5.7$  and the jet exit Reynolds number is approximately 5000. The measurements are focused on the developing region of the flow. Two flow configurations are studied, one in which the jet nozzle is flush with the tunnel wall and the other where the nozzle protrudes into the uniform region of the tunnel flow. The jet nozzle in both cases is a simple pipe. The averaged scalar and velocity fields show a strong similarity in growth rates and centreline decay rates between the two nozzle configurations when using the centreline downstream coordinate  $s$ . This suggests that the flow geometry is less important than, for example, jet exit conditions in determining the initial flow development. The velocity fields show indications of jet-like scaling in the near field, and a possible approach to wake-like scaling in the far field. These canonical scalings are less evident in the scalar fields. Results are presented for the averaged scalar variance,  $\langle C'^2 \rangle$ , the scalar flux components,  $\langle u'_i C' \rangle$ , the turbulent normal stresses,  $\langle u'^2 \rangle$  and  $\langle v'^2 \rangle$ , and the turbulent shear stress,  $\langle u'v' \rangle$ . We also discuss the resolution issues bearing on the determination of small-scale fluctuations.

---

## 1. Introduction

The crossflowing turbulent jet, in which a round jet is injected into a perpendicular fluid stream, has considerable practical significance in engineering systems. Combustion applications of this flow, for example, include aerospace propulsion, gas-burning power generation, and the on-site purging of excess gases at oil drilling sites. Many of these crossflowing jet applications involve mixing of molecular species or temperature. Efforts to model the dynamics of the crossflowing turbulent jet are described by Durando (1971), Broadwell & Breidenthal (1984), Karagozian (1986) and Hasselbrink & Mungal (1996, 2001*a*). Problems confronting modelling work include the complicated vortical structure of the flow, and the difficulty in modelling the near-field development. A diagram of the characteristic vortical structures of the crossflowing jet is given in figure 1. Shown are the horseshoe vortices that form at the windward side of the jet exit, the jet shear-layer instability (shown on the jet windward surface), the wake vortices, and the counter-rotating vortex pair (CVP). The CVP becomes the dominant structural feature of the crossflowing turbulent jet

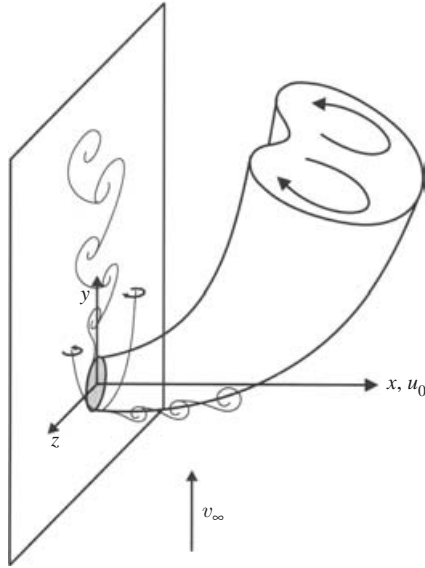


FIGURE 1. The vortical structure of the crossflowing jet.

as the flow develops, and accounts for much of the modelling difficulty. Experimental evidence also suggests that the flow is very sensitive to the ratio of jet velocity to crossflow velocity,  $r \equiv u_0/v_\infty$ , which constrains efforts to make general conclusions about the flow configuration.

The velocity and vorticity fields of the crossflowing turbulent jet have been the subject of many experiments. Much effort has focused on elucidating the structure of the vorticity field (including the work of Andreopoulos 1985; Fric & Roshko 1994; Kelso & Smits 1995; Kelso, Lim & Perry 1996; Rivero, Ferre & Giralt 2001). Pratte & Baines (1967) used flow visualization to determine jet trajectories and flow widths, and found that length scales are properly normalized by the factor  $rd$ , where  $d$  is the jet exit diameter. The measurements spanned a range of  $r$  values from 5 to 35. Crabb, Durão & Whitelaw (1981) mapped the mean flow of the crossflowing jet using both laser-Doppler and hot-wire anemometry, for  $r = 1.15$  and 2.3. Detailed measurements of the turbulent stresses, measured using hot wires, were reported by Andreopoulos & Rodi (1984) for flows with  $r = 0.5, 1$  and 2. This work also demonstrated that the jet exit velocity profile is strongly affected by the presence of the crossflow. Subsequently, Sherif & Pletcher (1989) also mapped the fields of turbulence quantities, for  $r = 2, 4$  and 6.

Despite the abundance of engineering applications involving molecular mixing, the body of work devoted to mixing in the crossflowing turbulent jet is relatively small. From measurements of velocities and jet fluid concentrations using probes in flows with  $r$  from 6.5 to over 50, Patrick (1967) showed that the points of maximum velocity penetrated further into the crossflow than the points of maximum concentration. Ramsey & Goldstein (1971) and Kamotani & Greber (1972) performed probe measurements of temperature in a heated (weakly buoyant) crossflowing jet in air, and reported that the mean temperature distribution in cross-sectional planes had a kidney-like structure akin to the signature of the CVP in the vorticity field. In these studies, the jet and crossflow fluid densities differ, so the jet-to-crossflow momentum ratio ( $r_m \equiv \rho_0 u_0^2 / \rho_\infty v_\infty^2$ , so  $r_m^{1/2} = r$  in the absence of density differences)

is the defining flow parameter; Ramsey & Goldstein (1971) investigated  $r_m$  values of approximately 0.01 to 4.7, while Kamotani & Greber (1972) presented results for  $r_m$  from 15 to 60. Andreopoulos (1983) performed simultaneous probe measurements of temperature and velocity, both the mean and fluctuating terms, in a heated non-buoyant crossflowing jet in air, for  $r=0.25, 0.5, 1$  and  $2$ . The results included measurements of the turbulent scalar (temperature) flux terms. With an eye to combustion applications, Birch *et al.* (1989) measured jet fluid concentrations, again using probes, for a methane jet injected into an air crossflow. Both non-reacting and reacting cases were considered, with values of  $r_m$  ranging from 100 to 2000.

Modern laser-imaging methods have also been applied to crossflowing jet mixing. Niederhaus, Champagne & Jacobs (1997) applied planar laser-induced fluorescence (PLIF) to obtain scalar concentration fields in cross-sections of crossflowing jets in water, with  $r=4.9$  to  $11.1$ . Applying PLIF in air-into-air crossflowing jets, Smith & Mungal (1998) mapped the concentration field in cross-sectional planes, the symmetry plane, and in planes parallel to the jet exit plane, for  $r$  ranging from  $5$  to  $20$ . Meyer, Özcan & Larsen (2002) implemented PLIF simultaneously with particle image velocimetry (PIV) in a crossflowing jet in water at  $r=3.3$ , allowing the determination of turbulent scalar fluxes in two-dimensional domains.

Progress toward simulating the crossflowing turbulent jet has accelerated in tandem with advances in computational power and algorithm development. Alvarez, Jones & Seoud (1993) described computations of crossflowing jets with  $r=0.5$  and  $2$ , including scalar mixing, using the Reynolds-averaged Navier–Stokes (RANS) approach. Accurate computation of the turbulent scalar flux terms was found to be particularly challenging. Large-eddy simulation (LES) is now being explored for crossflowing jet simulations, because of the inherent ability of the LES formulation to handle temporal unsteadiness and spatial complexity. Yuan, Street & Ferziger (1999) (also Yuan 1997; Yuan *et al.* 1998) computed jets with  $r=2$  and  $3.3$  using LES. The results faithfully reproduced the large-scale vortical structures of the flow, as well as statistics of fluctuation quantities, such as Reynolds stresses. The high sensitivity of the flow to jet inflow conditions was noted through explicit computation of the jet flow upstream of the exit. Interest in LES of the crossflowing jet is also driven by combustion applications. Schlüter & Schönfeld (2000) reported LES results for passive scalar mixing in crossflowing jets with  $r$  between  $2$  and  $6$ , paying particular attention to the effects of grid resolution and different subgrid models. That study also included the computation of a crossflowing jet in a realistic gas turbine burner geometry.

The present measurements are intended to provide a comprehensive view of the scalar and velocity fields in the developing region of the crossflowing turbulent jet in the gas phase, using planar imaging techniques. PLIF is used for the scalar field measurements, and PIV for the velocity field measurements. In order to evaluate the three-dimensionality of the flow, we perform the planar measurements in the centreplane (i.e. the jet symmetry plane) and at various positions off the centreplane. Prior crossflowing jet studies have identified a multitude of factors that affect the flow development, including the velocity (or momentum) ratio, and the jet initial velocity profile and Reynolds number. Here, we investigate instead the effect of the crossflow velocity profile, and the proximity of flow boundaries, by placing the jet nozzle exit both flush with the wind tunnel wall, and also outside the crossflow boundary layer. All measurements are made at a single jet-to-crossflow velocity ratio ( $r=5.7$ ) and jet exit Reynolds number ( $\approx 5000$ ). Velocity ratios of around  $5$  are of particular interest in aerospace propulsion applications.

A major goal of the present study is to determine the large-scale properties of both the scalar mixing and velocity fields in the crossflowing jet flow. These properties include the jet centreline trajectory, in the form  $x = \text{fn}(y)$ ; the jet width,  $\delta$ , in terms of the jet centreline coordinate,  $s$ ; and the velocity and scalar concentration decay on the centreline as functions of  $s$ . In analysing the scaling properties of the crossflowing jet, the flow may be divided into three regimes. In the near field, for sufficiently large  $r$ , the jet momentum dominates and the flow can be expected to approximate a pure jet. The flow then bends through an intermediate region until, in the very far field, memory of the initial conditions will be lost and the flow is expected to resemble a wake. However, whether the flow does attain this asymptotic state, and whether it displays self-similarity, are still unclear. The answers may depend, for example, on whether the nozzle exit is flush with a wall, as shown in figure 1, or is well away from any flow boundaries.

The present work also aims to provide a comprehensive mapping of the velocity and scalar fields in the crossflowing turbulent jet, suitable for assessment of ongoing computational efforts. The mapping of the flow is presented in terms of profiles of averaged quantities, along the jet initial direction and the crossflow direction. In addition to profiles of the mean scalar values and velocity components, we present profiles of the (averaged) scalar variance,  $\langle C'^2 \rangle$ , scalar flux components,  $\langle u' C' \rangle$ , turbulent normal stresses,  $\langle u'^2 \rangle$  and  $\langle v'^2 \rangle$ , and turbulent shear stress,  $\langle u' v' \rangle$ . Accurate reproduction of these small-scale fluctuation terms is essential for combustion applications, and poses a rigorous challenge for simulations.

The paper is organized as follows. Section 2 describes the experimental conditions. Discussion of the structure and scaling properties of the mean scalar and mean velocity fields are given in §3 and §4, respectively. Section 5 presents results from the turbulent fluctuations, and §6 summarizes the major conclusions of this work.

## 2. Experimental conditions

These experiments are performed in an updraft wind tunnel with air as crossflow fluid and nitrogen as jet fluid. The jet fluid is seeded with acetone vapour (molecular weight 58.08) to 10% by volume for diagnostic purposes, so the ratio between the jet fluid density,  $\rho_0$ , and the ambient fluid density,  $\rho_\infty$ , is 1.10. The tunnel cross-section measures  $50 \times 50 \text{ cm}^2$ . Two fine-mesh screens and one honeycomb section condition the tunnel flow. For the present experiments, the tunnel crossflow velocity profile has a peak value of  $v_\infty = 2.95 \text{ m s}^{-1}$ . The jet nozzle is a simple pipe with 6.35 mm outer diameter, inner diameter  $d = 4.53 \text{ mm}$ , and length 320 mm. In the absence of a crossflow, fully developed pipe flow conditions would prevail at the jet exit; the presence of the crossflow, however, is known to affect the jet exit profile (e.g. Andreopoulos & Rodi 1984). The jet exit velocity profile is not measured in these experiments. The average (bulk) jet velocity based on volumetric flow rate is  $u_0 = 16.9 \text{ m s}^{-1}$ , giving a velocity ratio  $r = 5.7$  and a jet exit Reynolds number of approximately 5000.

The binary diffusivity of acetone and air, at 300 K and 1 atm, is  $D = 0.104 \text{ cm}^2 \text{ s}^{-1}$  (Reid, Prausnitz & Poling 1987), so with the kinematic viscosity of air being  $\nu = 0.155 \text{ cm}^2 \text{ s}^{-1}$ , the Schmidt number,  $Sc \equiv \nu/D$ , of the system is 1.49. To seed the acetone vapour into the jet flow, the jet fluid is passed through a bubbler containing liquid acetone. The bubbler is maintained at a near-constant temperature by an open-loop water flow through tubing immersed in the acetone supply. During an

experimental run, the acetone level in the bubbler, and the seeding efficiency, slowly diminishes. The data processing procedure necessarily accounts for this (§ 2.2).

### 2.1. Optical arrangement

Particle image velocimetry (PIV) is used to measure the velocity fields whereas planar laser-induced fluorescence (PLIF) is used for the scalar field measurements. To provide the Mie scattering signal for particle image velocimetry, the jet flow is seeded with submicron aluminium oxide particles, while the crossflow is seeded with a glycerol–water fog produced by a commercial fog machine (Rosco 1500). A single, dual cavity Nd:YAG laser (Spectra-Physics PIV-400), with frequency-doubled 532 nm output, is used to produce two laser sheet pulses in quick succession. The time delay between pulses is as short as 8  $\mu$ s. The resulting scattering signal is collected by an interline transfer CCD camera (Kodak Megaplus ES 1.0, 1K $\times$ 1K pixel resolution), fitted with a 35 mm format Nikon 105 mm f/2.8 macro lens. The frame transfer capability of this camera allows each of the two closely spaced laser sheet pulses to be captured in a separate image. This permits the use of a cross-correlation PIV algorithm (Hasselbrink 1999), which eliminates directional ambiguity and yields improved resolution over single-image autocorrelation techniques. The algorithm used here also incorporates iterative interrogation window offset to increase vector yield.

For the laser-induced fluorescence, acetone is seeded into the jet fluid stream, to approximately 10% by volume. To excite the fluorescence signal, a XeCl excimer laser with 308 nm output (Lambda-Physik EMG 203MSC) is used. The PLIF signal is captured by a thermoelectrically cooled slow-scan CCD camera (Photometrics AT200), with 512  $\times$  512 pixel resolution. The imaging lens is a 35 mm format Nikon 50 mm f/1.2 lens, fitted with a +1 diopetre close-up lens for close focusing. Two 2 mm thick BG-25 bandpass filters isolate the PLIF signal (which peaks in the range 400–500 nm) from the much brighter Mie scattering signal at 532 nm. Post-processing of the PLIF data corrects for background light levels, non-uniformity in laser sheet intensity, and local laser intensity attenuation caused by passage of the sheet through the fluorescent medium. Experiment timing and synchronization are controlled by three Stanford Research Systems DG 535 pulse generators.

With the jet as depicted in figure 1, the vertically oriented laser sheets pass through the flow from right to left (from the  $+x$  to the  $-x$  direction). Prior to entering the measurement area, both the 532 nm and 308 nm laser beams pass through a focusing spherical lens (nominal focal length  $f = 1$  mm), a diverging cylindrical lens ( $f = -20$  mm) to form the sheets, and a converging cylindrical lens ( $f = 250$  mm) to control the sheet spreading angle. Special care is taken to ensure that the two laser sheets are spatially coincident throughout the measurement area. The centres of the two sheets are separated by no more than 50  $\mu$ m throughout the measurement area, where the thickness of the 532 nm sheet varies from approximately 300 to 800  $\mu$ m, and the thickness of the 308 nm sheet ranges from 500 to 1000  $\mu$ m.

### 2.2. Flow mapping

The aim of the present measurements is to provide a comprehensive picture of the mixing and velocity fields in the developing region of the turbulent crossflowing jet. The imaging planes are parallel to the plane of the crossflowing jet trajectory; the planar measurement area extends from the jet exit, and encompasses the onset of the region identified as the far field by Smith & Mungal (1998) on the basis of scalar measurements. To evaluate the three-dimensionality of the flow, the planar measurements are taken in the jet centreplane, as well as in planes located at 0.22*rd*,

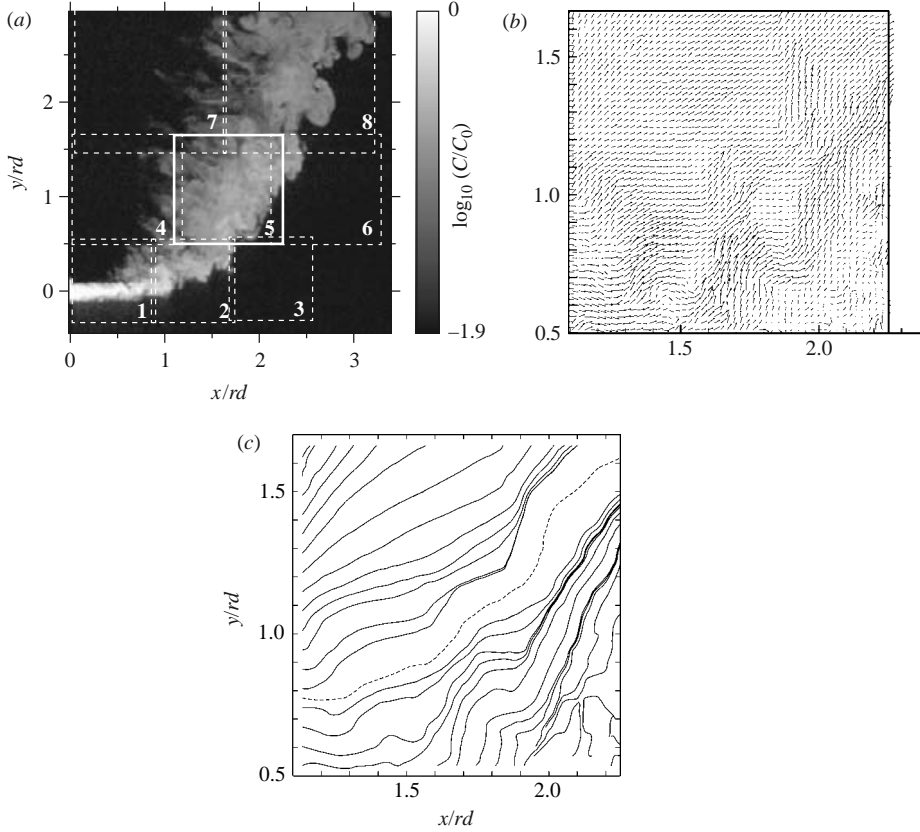


FIGURE 2. A sample image pair, from the centreplane of the protruding nozzle case. (a) The scalar field, showing the 8 imaging subwindows used for PIV. (b) The PIV vector field corresponding to the solid box (subwindow number 5) in (a). (c) The two-dimensional stream traces for the vector field in (b).

$0.45rd$ ,  $0.67rd$ ,  $0.89rd$  and  $1.11rd$  off the centreplane. Two jet nozzle positions are considered, the first in which the nozzle exit is flush with the wind-tunnel wall, and the second in which the nozzle protrudes 100 mm into the crossflow, allowing assesment of the effect of the crossflow boundary layer on the flow development. The 80% point of the boundary-layer profile lies 6 mm from the wind-tunnel wall, so, in this protruding nozzle case, the jet is well outside the crossflow boundary layer.

A sample PLIF image, taken in the centreplane with the protruding nozzle, is shown in figure 2(a). As shown in figure 1,  $x$  is the initial jet direction,  $y$  is the crossflow direction, and  $z$  is the out-of-plane direction. In these scalar measurements, it is necessary to include the jet potential core in the imaging region, to permit the correlation of measured signal levels with jet fluid concentration. The size of the scalar imaging region is then restricted by the desire to resolve fine-scale fluctuations in the scalar field in the  $512 \times 512$  pixel images. The resulting raw PLIF imaging window spans roughly  $3.5rd$  per side, and is identical for all of the measurements. In contrast, it is not required that the PIV images include the potential core for reference purposes. The PIV processing, however, inherently compromises resolution, yielding here a final vector resolution of  $100 \times 100$  pixels from the original  $1K \times 1K$  Mie scattering images. In order that the processed PIV results resolve fluctuations in

---

Nozzle position	$z$ ( $rd$ )	Total images	PIV subwindow (number of images)
Flush	0	821	1(105), 2(103), 3(89), 4(101), 5(101), 6(92), 7(98), 8(132)
	0.22	615	1(70), 2(71), 3(63), 4(74), 5(73), 6(68), 7(61), 8(135)
	0.45	478	1(40), 2(53), 3(39), 4(54), 5(68), 6(69), 7(66), 8(89)
	0.67	303	4(35), 5(67), 6(40), 7(68), 8(93)
	0.89	166	5(38), 7(55), 8(73)
	1.11	40	8(40)
100 mm	0	908	1(98), 2(102), 3(100), 4(100), 5(132), 6(155), 7(120), 8(101)
	0.22	595	1(74), 2(67), 3(65), 4(66), 5(87), 6(77), 7(75), 8(84)
	0.45	469	1(33), 2(49), 3(37), 4(79), 5(67), 6(72), 7(64), 8(68)
	0.67	309	4(52), 5(65), 6(51), 7(75), 8(66)
	0.89	167	5(49), 7(52), 8(66)
	1.11	36	8(36)

---

TABLE 1. Coverage of the measurement region by the PLIF and PIV imaging planes, with the jet nozzle positioned either flush with the tunnel wall or protruding 100 mm into the main flow. The spacing,  $z$ , between the measurement planes and the jet trajectory plane is given in multiples of  $rd$ . Shown is the total number of PLIF images at each  $z$  position. Each PLIF measurement has a corresponding PIV measurement taken in one of the eight subwindows shown in figure 2; also shown are the particular PIV subwindows, and the number of measurements in each subwindow, used for each of the positions  $z$ .

---

the velocity field, the full PLIF imaging region is tiled by eight smaller PIV imaging windows, as indicated by the dashed boxes in figure 2(a). For the particular scalar field shown in the figure, the simultaneous PIV field is given in figure 2(b), and corresponds to the solid box (subwindow number 5) in figure 2(a). (Figure 2(c) shows the two-dimensional stream trace pattern for the vector field in figure 2(b); this will be discussed further in § 4.1.) Table 1 summarizes the mapping of the flow for the full set of measurements. For  $z=0$ ,  $0.22rd$  and  $0.45rd$ , PIV measurements are made in the full set of eight subwindows indicated in figure 2(a), while for  $z=0.67rd$ ,  $0.89rd$  and  $1.11rd$ , PIV measurements are made only in those subwindows in which the flow is expected to be significantly affected by the presence of the jet.

All scalar field results are normalized by the scalar concentration value in the jet nozzle,  $C_0$ . For each image in the jet centreplane,  $z=0$ , the jet potential core is in view (e.g. figure 2) and we can determine  $C_0$  directly. For the off-centreplanes, however,  $C_0$  cannot be found in this way. Instead,  $C_0$  for those images was determined by extrapolating the known values from the  $z=0$  planes. The imaging measurements were performed in groups, having fixed nozzle position and PIV imaging subwindow; in each such group, sets of images were collected for the range of image plane locations  $z$ , beginning with  $z=0$ . The acetone bubbler was filled only prior to each measurement group. Recognizing that the value of  $C_0$  drops in absolute terms during the experiments as the acetone seeding efficiency drops (§ 2), the decay rate of  $C_0$  was measured explicitly. We determined the  $C_0$  decay rate to be  $\Delta C_0/\Delta T \approx -0.00034$ , normalized such that  $C_0=1.0$  initially, and where  $\Delta T$ , the time between successive images, was 16 s. The appropriate  $C_0$  for the  $z \neq 0$  imaging planes was then found using this value of  $\Delta C_0/\Delta T$ . (Power fluctuations in the excimer laser light source can also affect  $C_0$ ; however, for these measurements, the averaged laser pulse power was essentially constant over the course of each measurement group.)

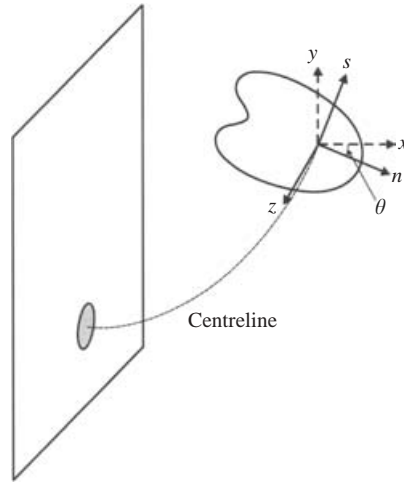


FIGURE 3. The  $(s, n, z)$  and Cartesian coordinate systems. The systems are related by rotation about the  $z$ -axis through the angle  $\theta$ .

### 2.3. Coordinate systems

In analysing the crossflowing jet, it is sometimes preferable to use a coordinate system that reflects the downstream evolution of the flow. Given knowledge of the flow centreline, we define  $s$  as the coordinate along this centreline, and  $n$  as normal to the centreline, where the  $(s, n)$ -plane is the same as the Cartesian  $(x, y)$ -plane (figure 3). The  $z$ -coordinate is the same in both coordinate systems. The positive- $n$  side of the jet is referred to as the windward side, and the positive- $n$  boundary is also called the jet outer boundary, while the negative- $n$  side of the jet is known as the lee or wake side, and the negative- $n$  boundary is also called the jet inner boundary.

An intuitive definition of the flow centreline is in terms of the *centre streamline*, namely the streamline, determined from the mean flow field, that originates in the centre of the nozzle exit. However, other centreline definitions are possible, for example, using scalar or velocity field magnitudes. In this paper, where the  $(s, n, z)$  coordinate system is used, the particular definition of the centreline will be clearly indicated.

## 3. Scalar field structure and scaling

Samples of instantaneous scalar fields, for the flush nozzle flow configuration, are shown in figure 4. The fields shown are for the jet centreplane ( $z=0$ ), as well as the planes  $z=0.22rd$ ,  $0.45rd$  and  $0.67rd$ . All scalar fields are normalized by  $C_0$ , the jet nozzle scalar concentration. The  $z=0$  scalar field shown is typical in that the jet scalar boundary on the lee side (the  $-x$  side) is marked by thin scalar filaments, which are aligned normal to the jet trajectory. These filaments probably correspond with the wake vortices that form when the uniform crossflow encounters the jet near field (figure 1). The lee-side jet boundary for the  $z \geq 0.22rd$  measurement planes shows essentially no evidence of these filaments, suggesting that the individual wake vortices remain closer to the centreline within the measurement area. Scalar fields for the protruding nozzle case are qualitatively similar to those of figure 4; the slight, though noticeable, differences are that typical scalar fields for the flush nozzle case both penetrate further into the crossflow, and spread into the  $z > 0$  planes nearer to the nozzle exit.

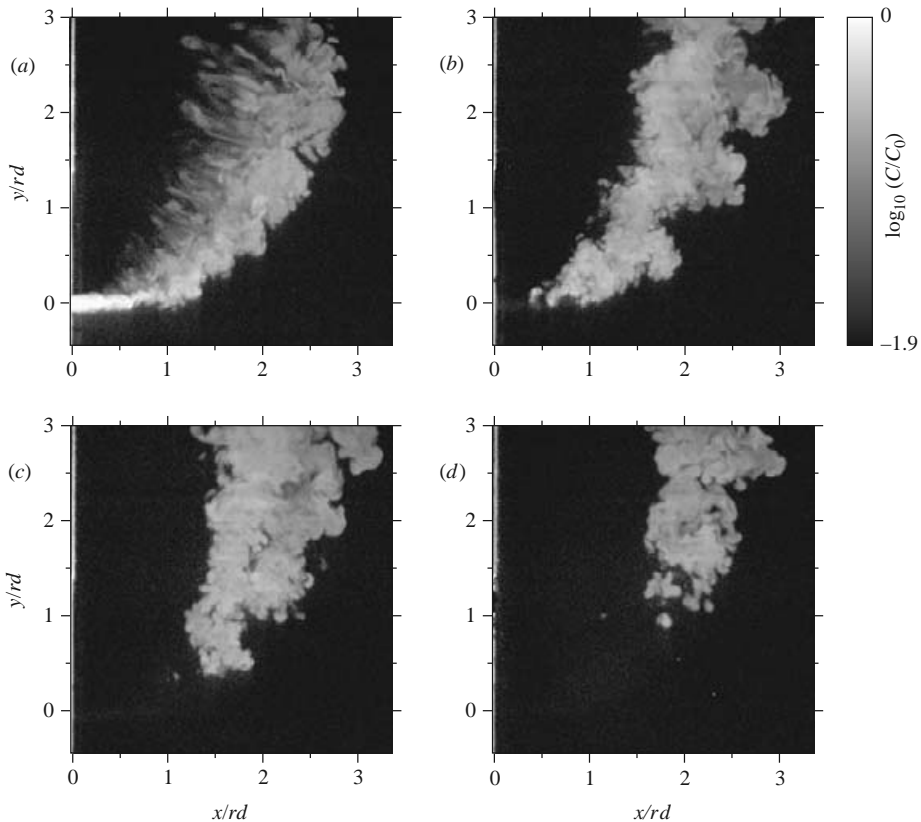


FIGURE 4. Sample scalar fields for the flush nozzle case, for (a)  $z=0$  (the jet centreplane), (b)  $z=0.22rd$ , (c)  $z=0.45rd$  and (d)  $z=0.67rd$ . Values are normalized by the initial jet concentration  $C_0$ .

Figure 5 shows the mean scalar fields,  $\langle C \rangle$  (where  $C = \langle C \rangle + C'$ ), for the flush nozzle case, again in the planes  $z=0, 0.22rd, 0.45rd$  and  $0.67rd$ . The averages are compiled over 821, 615, 478 and 303 images for the respective  $z$ -positions (table 1). Again, the mean scalar fields for the protruding nozzle position (not shown) are qualitatively similar to the flush nozzle fields, with the differences being the same as those identified in the instantaneous fields.

### 3.1. Flow trajectory

The mean scalar fields as shown in figure 5 are first used to quantify the jet development in terms of the scalar flow trajectories. We define the *scalar centreline* as the locus of points of maximum mean scalar concentration along trajectory-normal profiles. The scalar centreline is found by first determining the points of maximum mean scalar concentration along fixed- $x$  profiles in the jet near field, and fixed- $y$  profiles in the far field of the measurement region, then using this tentative trajectory to define the trajectory-normal profile directions. The maximum mean scalar values on those profiles then define the scalar centreline.

Figure 6 shows the jet development in terms of the scalar centreline trajectory in the centreplane, for both the flush and protruding nozzle cases. The figure shows the tendency of the jet issuing from the flush nozzle to impinge further into the crossflow.

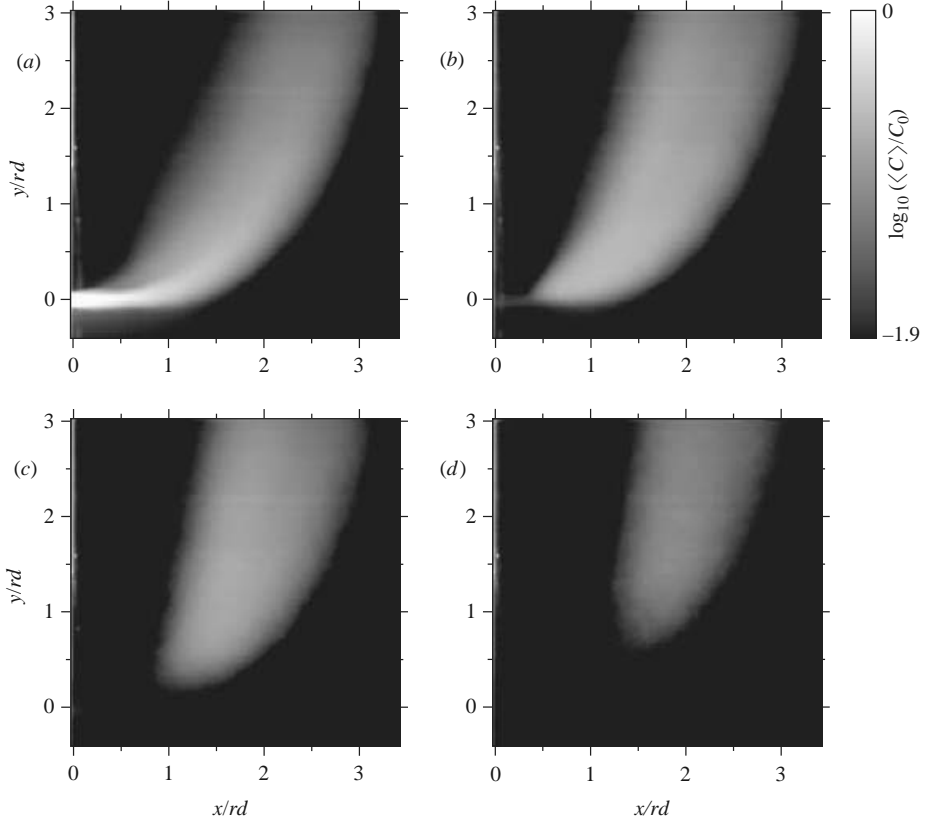


FIGURE 5. The mean scalar field for the flush nozzle case, in the planes (a)  $z=0$ , (b)  $z=0.22rd$ , (c)  $z=0.45rd$  and (d)  $z=0.67rd$ .

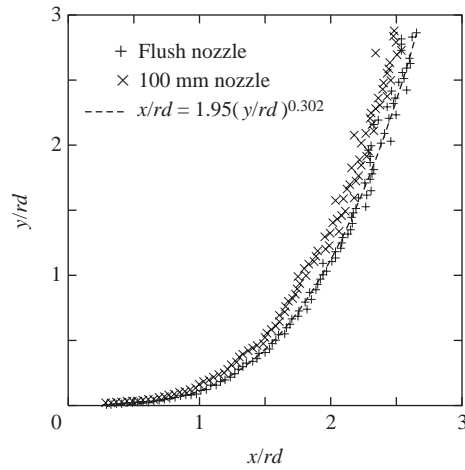


FIGURE 6. Scalar centreline trajectories in the jet centreplane ( $z=0$ ). The dashed line is the fit to the flush nozzle data of equation (3.1).

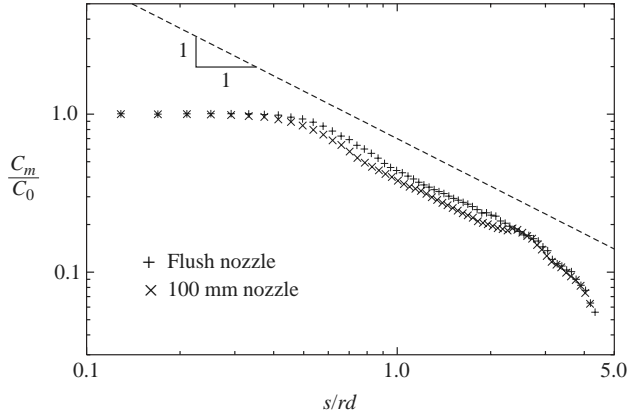


FIGURE 7. The decay of maximum mean scalar concentration with downstream distance in the centreplane, for both the flush and protruding nozzles. The coordinate  $s$  is the coordinate along the scalar centreline, as defined by (3.1).

The dashed line is a least-squares fit to the flush nozzle data of the function

$$(x/rd) = A(y/rd)^m, \quad (3.1)$$

with  $A = 1.95$  and  $m = 0.302$ . The fit to the protruding nozzle data gives  $A = 1.81$  and  $m = 0.323$ . The tendency of the flow in the flush nozzle case to penetrate further into the crossflow can be intuitively explained by noting that in that case, the jet initially flows through low-momentum fluid in the crossflow boundary layer. The analysis of velocity field trajectories suggests that the picture may be more complex, however (see following section).

### 3.2. Centreline decay and flow width

The decay of the maximum scalar concentration in the centreplane, for both the flush and protruding nozzle cases, is shown in figure 7. The data are plotted in terms of the scalar centreline downstream coordinate,  $s$ , which is determined through numerical integration of the best-fit trajectories defined by (3.1). Beyond the potential core, the maximum concentration  $C(s)$  decays roughly as  $1/s$ , which is the decay dependence seen in simple jets. This contrasts with the results of Smith & Mungal (1998), for values of  $r$  ranging from 5 to 25, who found an initial decay faster than  $1/s$ . Those earlier results also showed distinct branch points where the concentration decay abruptly slowed, possibly to an  $s^{-2/3}$  dependence which would indicate wake-like behaviour. However, the present data show a decay rate which actually increases beyond  $s/rd \approx 2.5$ . Also of interest is the agreement between the flush and protruding nozzle cases when the data are plotted in this centreline coordinate. The functional dependences of the decay curves are similar, as is the point at which the decay rate increases beyond  $1/s$ , though the potential core in the flush nozzle case penetrates further into  $s$  space.

Figure 8 shows the dependence of the flow widths on the scalar centreline coordinate  $s$ . The flow nominal half-width for a given  $s$  is computed by first determining the maximum concentration,  $C(s)$ , then moving in the trajectory-normal direction until the concentration drops to a specified fraction (here, 20%) of  $C(s)$ . Because the flow is not symmetric about the centreline trajectory in the imaging plane, it is necessary to compute these partial widths separately for both the  $-x$  direction (i.e. towards the wake region) and the  $+x$  direction (towards the jet outer boundary). We denote

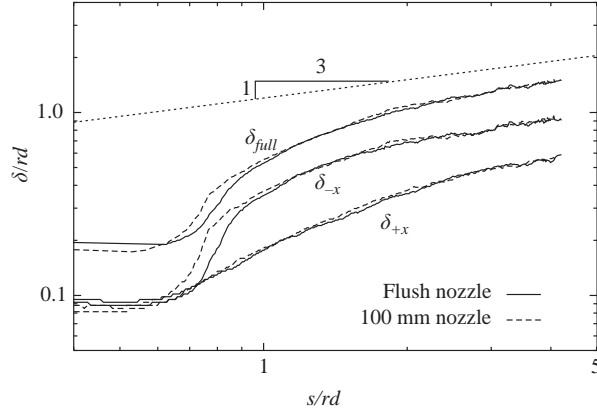


FIGURE 8. Mean scalar field flow width in the centreplane as a function of the scalar centreline coordinate,  $s$ , for both nozzle positions. The quantity  $\delta_{full}$  is the flow width in the trajectory-normal direction,  $n$ , between points where the scalar value is 20% of the maximum;  $\delta_{-x}$  and  $\delta_{+x}$  are the associated partial widths measured from the centreline toward the wake region and the jet outer boundary, respectively.

these partial widths by  $\delta_{-x}$  and  $\delta_{+x}$ , and the full width by  $\delta_{full} \equiv \delta_{-x} + \delta_{+x}$ . Figure 8 shows the results for  $\delta_{-x}$ ,  $\delta_{+x}$  and  $\delta_{full}$  as functions of  $s$ . The lack of symmetry, with  $\delta_{-x} > \delta_{+x}$ , is clear. This asymmetry is due to jet fluid that is stripped away from the developing region of the jet by the crossflow and is deposited in the wake region. Jet fluid is present in the wake region even near the nozzle (small  $s$ ), as can be seen in both the instantaneous and mean scalar fields (figures 4 and 5). As a result, just outside of the potential core, the growth rate of  $\delta_{full}$  exceeds  $\delta \propto s$ , the linear growth observed in pure jets. For higher values of  $s$ , the  $\delta_{full}$  curve shows evidence of an asymptotic approach to an  $s^{1/3}$  dependence, which would correspond to a wake-like scaling. Finally, the curves for both the flush and protruding nozzle cases are in good agreement for  $s/rd > 1$ , again showing the similarity in flow development for the two configurations when the centreline coordinate  $s$  is used.

### 3.3. Three-dimensionality in the scalar field

Whereas the flow width,  $\delta_{full}$ , appears for both the flush and protruding nozzle cases to be approaching a dependence on the centreline coordinate,  $s$ , consistent with a wake-like scaling, the concentration decay does not. These scaling laws rely upon self-similarity in the mean profiles, so it is reasonable to look to a lack of self-similarity to explain the departures from wake scaling seen in the data. The three-dimensionality of the flow will also be important. Figure 9 shows the maximum mean scalar concentration as a function of  $s$  for the jet centreplane, as well as for planes located  $0.22rd$ ,  $0.45rd$ ,  $0.67rd$  and  $0.89rd$  off of the centreplane. The data are for the flush nozzle case; the protruding nozzle data are qualitatively similar. The coordinate  $s$  for all of these curves is determined from the jet scalar centreline trajectory in the centreplane, and the maximum mean scalar values,  $C_m$ , are those along the profile in the  $n$ -direction (the in-plane trajectory-normal direction). Of particular note in the figure is that the highest scalar concentration is not found in the centreplane for  $s/rd > 2.2$ . Instead, the jet cross-section takes on a bimodal profile in which the scalar maxima lie off of the centreplane. This is sufficient to explain the deviation from a wake-like concentration decay in the centreplane, because the wake similarity profile has its peak on the centreline.

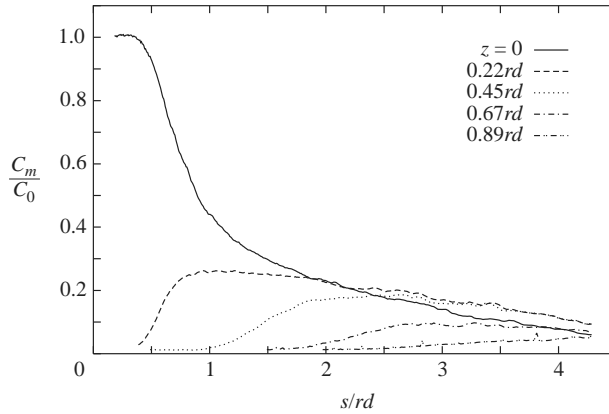


FIGURE 9. The decay of maximum mean scalar concentration,  $C_m$ , with downstream distance, for the measurement planes  $z=0$ ,  $0.22rd$ ,  $0.45rd$ ,  $0.67rd$  and  $0.89rd$ . Data for the flush nozzle case.

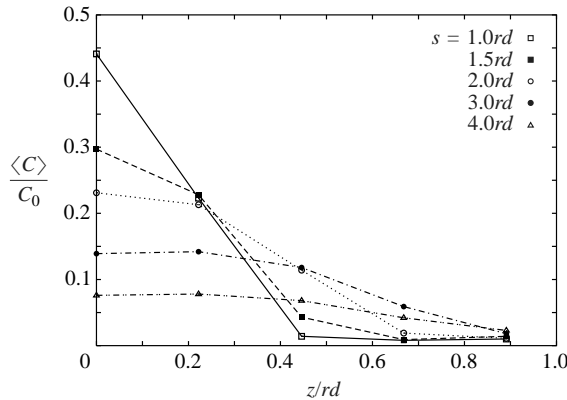


FIGURE 10. Mean scalar concentration values on the scalar centreline as functions of the  $z$ -coordinate, for fixed  $s = 1.0rd$ ,  $1.5rd$ ,  $2.0rd$ ,  $3.0rd$  and  $4.0rd$ , and  $n=0$ . Data for the flush nozzle case.

Figure 10 shows the profiles of mean scalar values in the  $z$ -direction, for different values of the scalar centreline coordinate,  $s$ , and  $n=0$ . The lack of similarity in these profiles is clear; in particular the  $s = 3.0rd$  and  $4.0rd$  profiles have higher  $\langle C \rangle$  values at  $z=0.22rd$  than in the centreplane. The tendency of the maximum mean scalar values to be achieved at  $z > 0$  is, however, less pronounced in these  $z$ -profiles than in the decay curves of Fig. 9, because the  $z$ -profiles are for  $n=0$ , and (as will be seen below, in Fig. 12) the scalar maxima in the off-centre,  $z > 0$  planes lie at  $n < 0$ .

Figure 11 presents a different view of the three-dimensionality of the scalar field. Shown are the boundary contours for the scalar field in the centreplane and in the  $z=0.22$ ,  $0.45rd$ ,  $0.67rd$  and  $0.89rd$  planes, together with the scalar centreline trajectory for the centreplane. The contours represent the loci of points in a given scalar trajectory-normal plane where the local scalar value is 20% of the maximum scalar value in the centreplane. On the outer boundary of the flow (i.e. the positive  $x$  side of the centreline), the deepest penetration occurs in the centreplane, with progressively shallower penetration for increasing off-centre position  $z$ . Meanwhile,

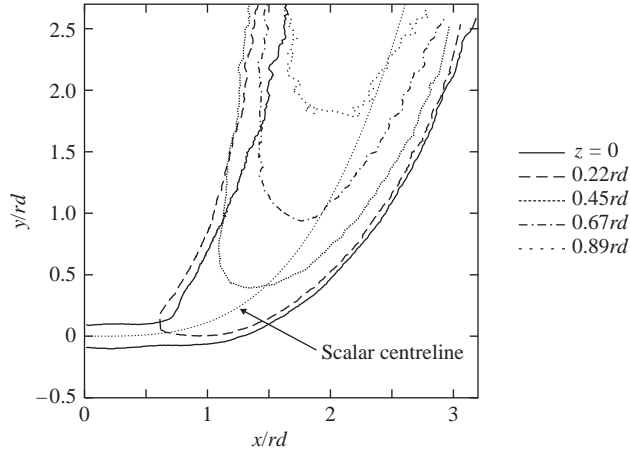


FIGURE 11. Boundary contours for the mean scalar field. The curves represent the loci of points in a given scalar trajectory-normal plane (i.e. fixed  $s$ ) where the local mean scalar value is 20% of the maximum value in the centreplane. Data for the flush nozzle case.

on the wake side of the flow, with increasing  $y$ , the boundaries for the off-centreplanes all lie further from the centreline trajectory than does the boundary in the centreplane. This corresponds to a kidney-like shape of the flow cross-section, as depicted in figure 1. This cross-sectional shape arises because of the dominant role played by the counter-rotating vortex pair (CVP) in the large-scale organization of the flow.

Figure 12 illustrates the cross-sectional form of the mean scalar field, in the form of profiles of  $\langle C \rangle$  along the trajectory-normal direction,  $n$ , in the different  $z$ -planes. Shown are the profiles for  $s = 2.0rd$ ,  $3.0rd$  and  $4.0rd$ . The  $n$ -coordinate is defined as positive toward the jet outer boundary (figure 12a). The kidney-like form of the cross-section is evident in that the  $\langle C \rangle$  profiles for  $z = 0.22rd$  are broader than the  $z = 0$  profiles, for the three  $s$  values shown; for  $s = 3.0rd$  and  $4.0rd$ , the  $z = 0.45rd$  profiles are also broader than the profiles in the centreplane. Also, while the peaks of the  $\langle C \rangle$  profiles in the  $z = 0$  plane lie by definition at  $n = 0$ , figure 12 also shows clearly that the profile peaks for  $z > 0$  lie toward the wake side of the flow ( $n < 0$ ).

The current measurements show good agreement in decay rates and flow widths (when expressed in terms of the scalar centreline coordinate  $s$ ) between the flush and protruding nozzle cases, yet the decay rates differ from those reported by Smith & Mungal (1998), whose results were consistent over a range of velocity ratios  $r$ . The most notable difference is that Smith & Mungal used a top-hat jet exit velocity profile while the present data use a pipe flow profile. The conclusion drawn here is that the jet exit profile plays a larger role in establishing the scaling properties of the mixing field than does the jet nozzle position or the value of  $r$ . This result is supported by the idea that the development of the counter-rotating vortex pair, which dominates the far-field flow structure, is highly dependent on vorticity introduced at the nozzle (e.g. Haven & Kurosaka 1997).

### 3.4. Mean scalar field $x$ - and $y$ -profiles

From the results for the mean scalar fields, we can also compile profiles through the jet in the  $(x, y)$ -plane. Profiles in Cartesian coordinates should facilitate comparisons

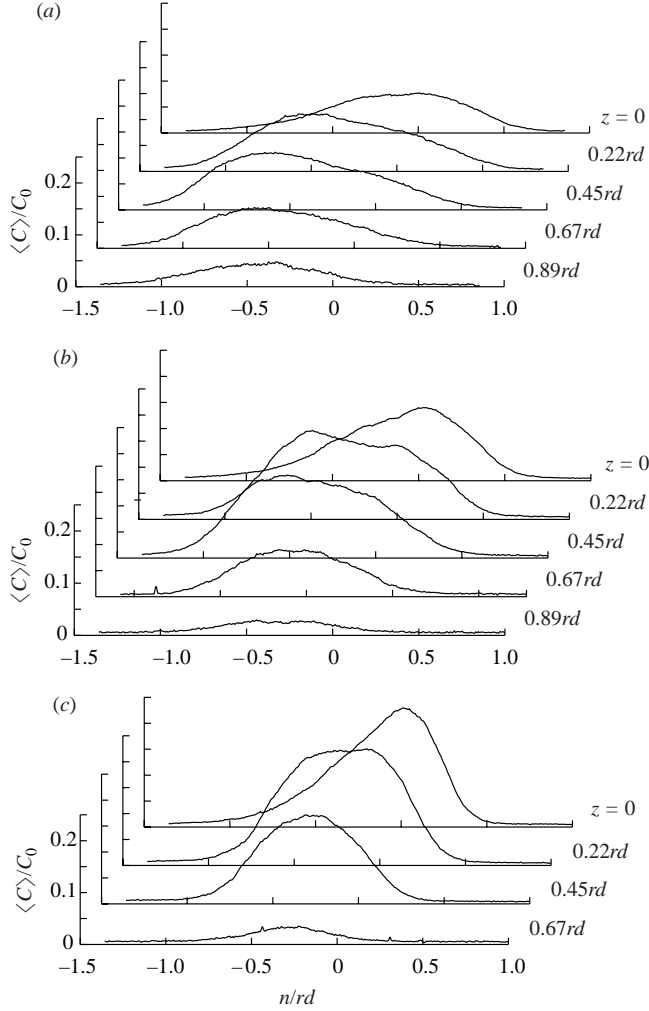


FIGURE 12. Profiles of mean scalar concentration along the trajectory-normal coordinate,  $n$ , in the different  $z = \text{const}$  measurement planes, for (a)  $s = 4.0rd$ , (b)  $s = 3.0rd$  and (c)  $s = 2.0rd$ . Data for the flush nozzle case.

with other existing or future computational or experimental results. Figure 13 presents profiles of  $\langle C \rangle$  in the jet centreplane for both the flush and protruding nozzle cases, along lines of fixed  $y = 0.5rd, 1.0rd, 1.5rd$  and  $2.5rd$ , and fixed  $x = 0.1rd, 0.5rd, 1.0rd$  and  $1.5rd$ . The profiles are compiled as averages over nine adjacent rows or columns in the  $512 \times 512$  data planes, so each profile actually represents a thin band through the data, extending  $\pm 0.027rd$  from the nominal fixed  $x$  or  $y$  value. Because these profiles are in Cartesian coordinates, rather than coordinates defined by the scalar trajectory, any comparisons of the different profiles (for example, to assess similarity) must recognize that the profiles are not transverse to the direction of flow evolution.

We can quantify the discrepancy between the fixed- $x$  and  $y$  profiles and the true local scalar trajectory-normal direction,  $n$ , by defining the flow trajectory in terms of the maximum scalar concentration, as in §3.1, and using the best-fit curves  $(x/rd) = 1.95(y/rd)^{0.302}$  for the flush nozzle data and  $(x/rd) = 1.81(y/rd)^{0.323}$  for the

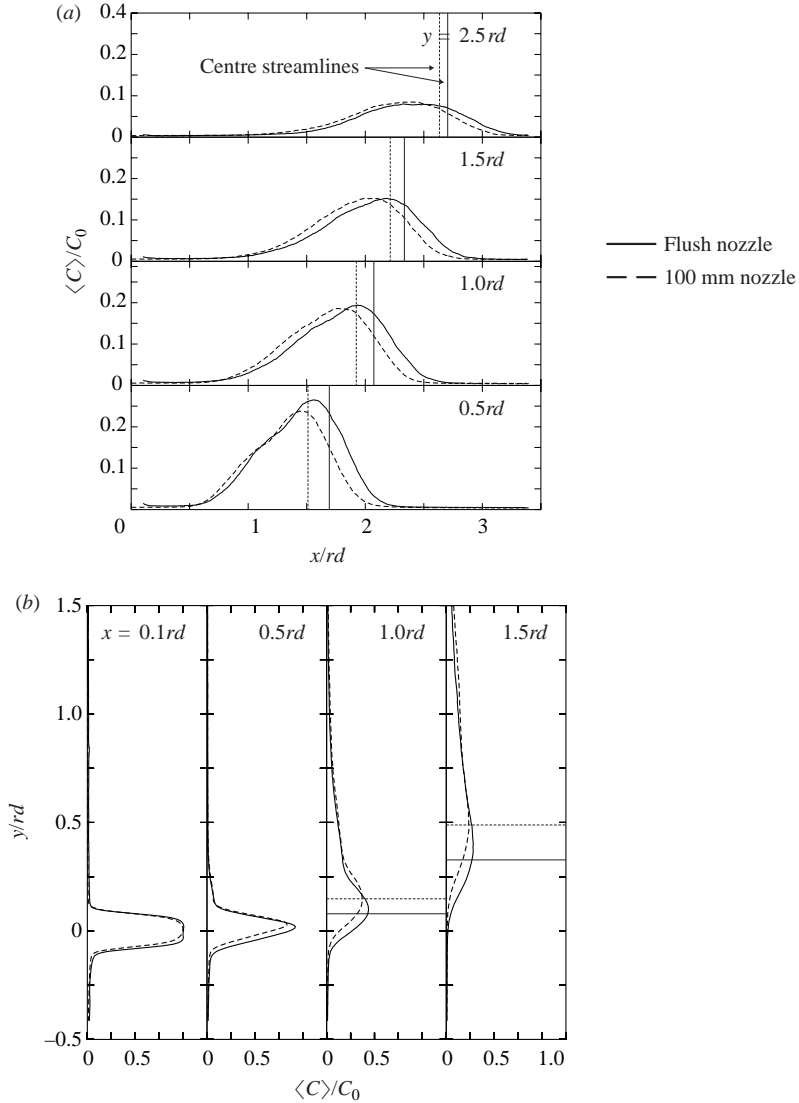


FIGURE 13. Averaged scalar field profiles in the jet centreplane, for both the flush and protruding nozzle cases. (a) The profiles for  $y=0.5rd$ ,  $1.0rd$ ,  $1.5rd$  and  $2.5rd$ , and (b) the profiles for  $x=0.1rd$ ,  $0.5rd$ ,  $1.0rd$  and  $1.5rd$ . Also indicated on the plots are the centre streamlines for the two nozzle positions (§4.2).

protruding nozzle data. Table 2 shows the angle,  $\theta$ , between the local scalar trajectory-normal direction and the profile direction for each of the profiles in figure 13. This  $\theta$  is simply the rotation angle defined in figure 3. Just outside the jet exit,  $\theta=0$ ; by  $x=1.0rd$ ,  $\theta=20^\circ$  for the flush nozzle and  $26^\circ$  for the protruding nozzle, as the flow bends in the crossflow direction; for both nozzle positions,  $\theta=24^\circ$  at  $y=1.5rd$ , dropping to  $17^\circ$  at  $y=2.5rd$ , as the jet flow increasingly aligns with the crossflow.

The profiles at  $x=0.5rd$  are symmetric around the position of peak concentration, except for a slight elevation in the tails on the positive- $y$  side, representing jet fluid that has been advected into the wake region on the lee side of the jet. The  $x=1.0rd$

---

Nozzle	$x/rd$ :	0.1	0.5	1.0	1.5	$y/rd$ :	0.5	1.0	1.5	2.5
Flush		0	4°	20°	43°		44°	30°	24°	17°
100 mm		0	7°	26°	49°		43°	30°	24°	17°

---

TABLE 2. The angle  $\theta$  between the local scalar trajectory-normal directions and the profile directions, for the profiles given in figure 13.

profiles show similar properties, though the increased scalar concentration in the wake region is more pronounced. For example, the profile for the flush nozzle case at  $x = 1.0rd$  is bell-shaped for  $y/rd \lesssim 0.25$ , with the wake becoming prominent for higher  $y$ . By  $x = 1.5rd$ , the profiles give no hint of symmetry. The nature of the asymmetry in these fixed- $x$  profiles would not be significantly affected by compiling the profiles in the directions normal to the true scalar trajectory. The centreline scalar concentration was seen in figure 7 to be consistent with pure jet scaling in the near field; however, the scalar field flow widths in figure 8, and the fixed- $x$  profiles in figure 13, show no evidence of jet-like self-similar evolution in the near field of these crossflowing jets.

The fixed- $y$  profiles in figure 13 are also noticeably asymmetric, with the peak  $\langle C \rangle$  values lying to the windward side of the profiles for  $y = 0.5rd$ ,  $1.0rd$  and  $1.5rd$ , as also seen in figure 12. By  $y = 2.5rd$ , the asymmetry seems to be reduced, though the flow partial-widths shown in figure 8 demonstrate that the asymmetry is significant even at the downstream limit of the measurement area. The flow full-widths shown in figure 8 do give some indication that these crossflowing jets are approaching a wake-like scaling, though the asymmetric fixed- $y$  profiles in figure 13, and the centreline concentration decay in figure 7, argue that these crossflowing jets have not achieved the self-similar wake limit within the measurement area.

Figure 14 shows the averaged scalar field profiles for both the flush and protruding nozzle cases in the  $z = 0.22rd$  plane. Comparing these profiles with those in the centreplane (figure 13) reinforces the point illustrated earlier by figure 12, namely that the maximum scalar magnitudes lie off the centreplane. The profiles in the  $z = 0.22rd$  plane are asymmetric throughout the measurement region, with the peak  $\langle C \rangle$  values lying on the windward side of the profiles in the near field (notably the  $x = 0.5rd$  and  $1.0rd$  profiles). As also seen in figure 12, the peak  $\langle C \rangle$  values then move to the wake side further downstream (the fixed- $y$  profiles). The  $\langle C \rangle$  profiles in the  $z = 0.45rd$  plane, given in figure 15, show the same asymmetry as do the profiles for  $z = 0.22rd$ .

The profiles for both nozzle configurations are in excellent agreement at the maximum downstream location ( $y = 2.5rd$ ) in the  $z = 0.45rd$  plane, and are in good agreement at  $y = 2.5rd$  in the  $z = 0$  and  $0.22rd$  planes. This observation supports the notion that the jet nozzle position does not have a significant effect on the asymptotic state of the flow, which was also concluded in §3.3 on the basis of the scaling properties of the flow.

#### 4. Velocity field structure and scaling

Figure 16 shows the the averaged velocity magnitude fields for the protruding nozzle case, in the jet centreplane,  $z = 0$ , and in the planes  $z = 0.22rd$ ,  $0.45rd$  and  $0.67rd$ . As mentioned in §2.2, these full fields are composed of eight subwindows. For the  $z = 0.67rd$  plane, no velocity measurements were performed in the subwindows labelled 1–3 in figure 2. The crossflow speed,  $v_\infty$ , has been subtracted from the vertical

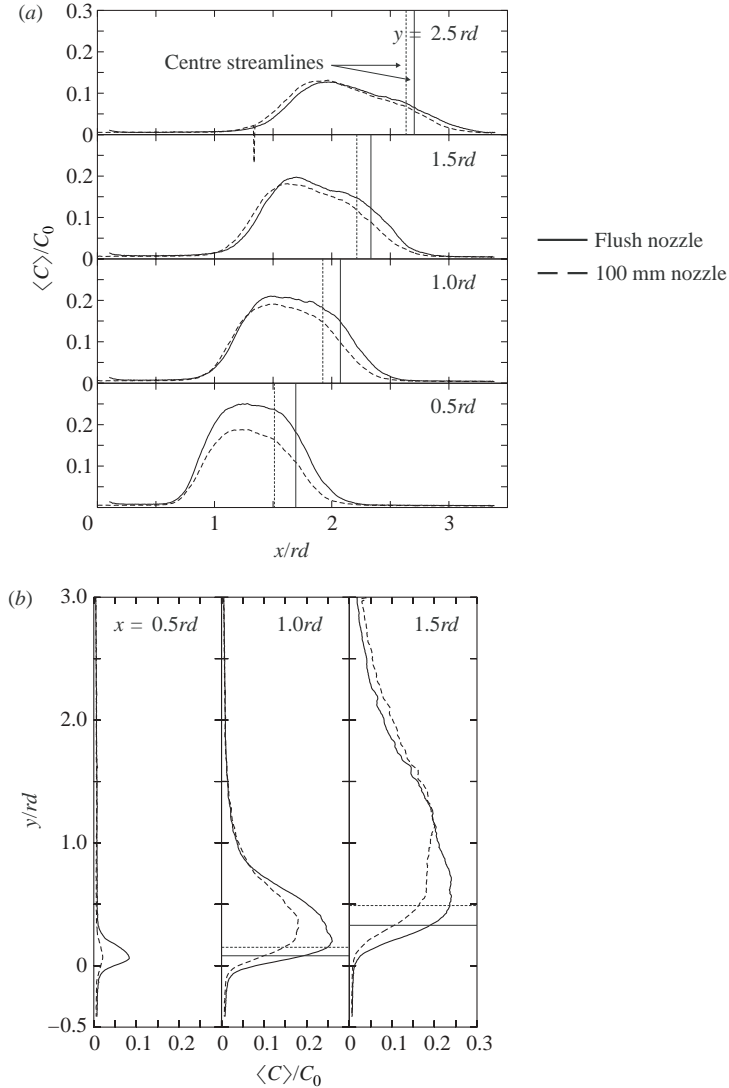


FIGURE 14. Averaged scalar field profiles in the  $z=0.22rd$  plane, for both the flush and protruding nozzle cases. (a) The profiles for  $y=0.5rd, 1.0rd, 1.5rd$  and  $2.5rd$  and (b) the profiles for  $x=0.5rd, 1.0rd$  and  $1.5rd$ .

velocity component in these figures. A minimum of 98 images were averaged for each subwindow in the centreplane, and more than 65, 33 and 51 images were averaged in each subwindow in the  $z=0.22rd, 0.45rd$  and  $0.67rd$  planes, respectively (table 1).

In figure 16(a) it is apparent that the region of large velocity magnitudes has a bifurcated structure, with one branch appearing to evolve from the initial jet trajectory, while the other branch turns more sharply into the wake region of the jet. This contrasts with the averaged scalar field of figure 5(a), in which the highest values follow a single trajectory. The bifurcated structure is also evident in the raw velocity magnitude fields computed without crossflow subtraction. This issue will be explored in §4.2.

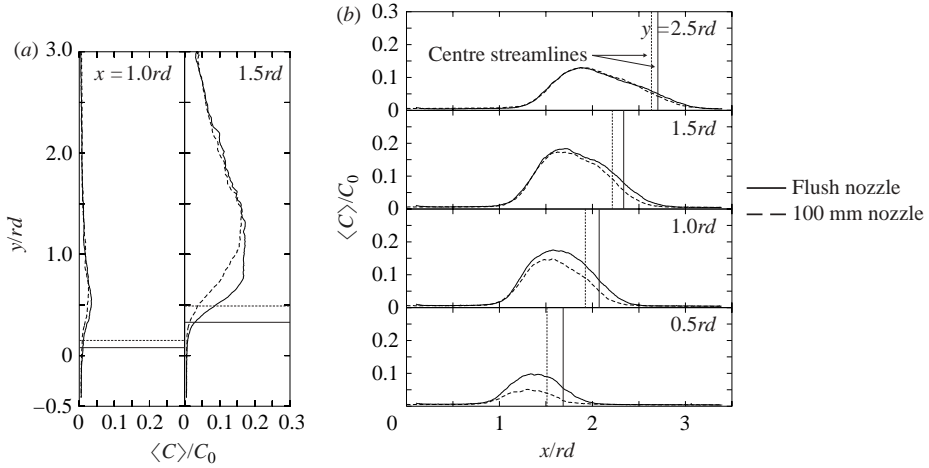


FIGURE 15. Averaged scalar field profiles in the  $z = 0.45rd$  plane, for both the flush and protruding nozzle cases. (a) The profiles for  $x = 1.0rd$  and  $1.5rd$ , and (b) the profiles for  $y = 0.5rd, 1.0rd, 1.5rd$  and  $2.5rd$ .

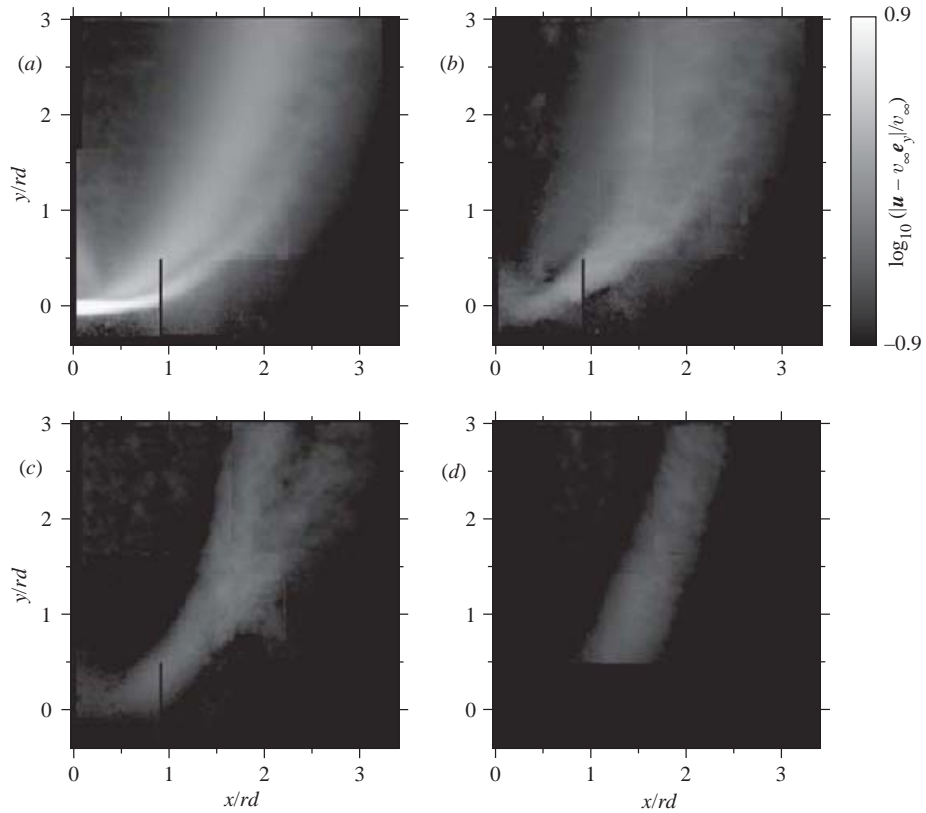


FIGURE 16. The mean velocity magnitude field for the protruding nozzle case, with the crossflow speed  $v_\infty$  subtracted from the vertical velocity component, in the planes (a)  $z = 0$ , (b)  $z = 0.22rd$ , (c)  $z = 0.45rd$  and (d)  $z = 0.67rd$ . For the  $z = 0.67rd$  plane, velocity measurements were not performed in subwindows 1–3 (figure 2).

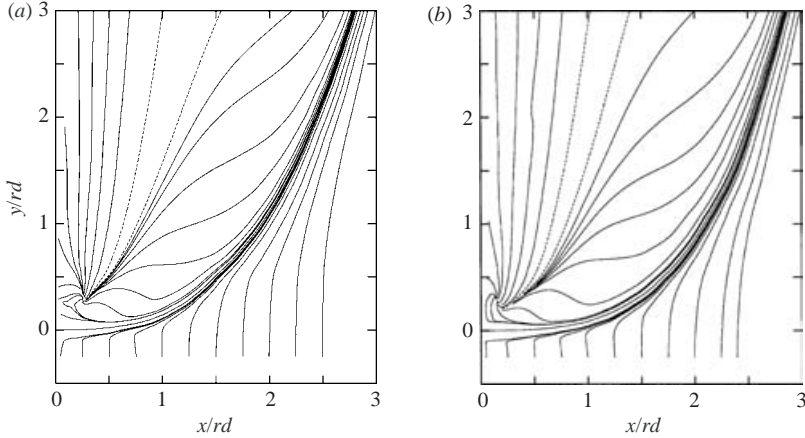


FIGURE 17. Two-dimensional streamlines determined from the mean velocity field results in the centreplane, for (a) the protruding nozzle case and (b) the flush nozzle case.

The mean velocity magnitude fields for the flush nozzle configuration (not shown) are qualitatively similar to those for the protruding nozzle configuration shown in figure 16. The apparent differences echo those noted in comparing the mean scalar fields for the two nozzle positions (§3); the velocity magnitude field for the flush nozzle case initially penetrates further into the crossflow, and more rapidly spreads from the  $z = 0$  plane.

#### 4.1. Two-dimensional streamlines

It is, perhaps, more intuitive to visualize velocity fields in terms of stream trace patterns. Figure 2(c) showed instantaneous, two-dimensional stream traces corresponding to the scalar and velocity vector fields shown in figures 2(a) and 2(b). Each stream trace shown in figure 2(c) is computed using a fourth-order Runge–Kutta path integration through the instantaneous velocity field. The flow pattern shows a general ‘waviness’ throughout most of the measurement window in figure 2(c). Additional complexity is evident at the lower right-hand side of the window, near the jet outer boundary, though the vector plot of figure 2(b) indicates that the in-plane velocity components are small in that region. The dashed trace in figure 2(c) indicates an area in the window where the traces diverge rapidly, probably due to significant three-dimensionality in the flow. It has been noted previously (Hama 1962) that relatively simple wavy flow patterns such as those in figure 2(c) can result in efficient mixing and highly convoluted scalar fields.

To compare the mean velocity fields for the protruding and flush nozzle cases, figure 17 shows the averaged velocity fields in the centreplane, for both nozzle configurations, in terms of their patterns of two-dimensional stream traces. Although only two velocity field components are available from the PIV, the computed traces in figure 17 represent actual flow streamlines, because the mean out-of-plane velocity component is zero in the centreplane, by symmetry. The initial points for the streamlines are chosen arbitrarily, so the spacing between the streamlines shown does not necessarily reflect their relative streamfunction values. The streamline patterns for the two nozzle positions are qualitatively very similar. In the jet near field ( $x \rightarrow 0$ ), both patterns show a stagnation point with positive two-dimensional divergence to the lee side (positive  $y$ ); in contrast, to the windward side (negative  $y$ ), there is no

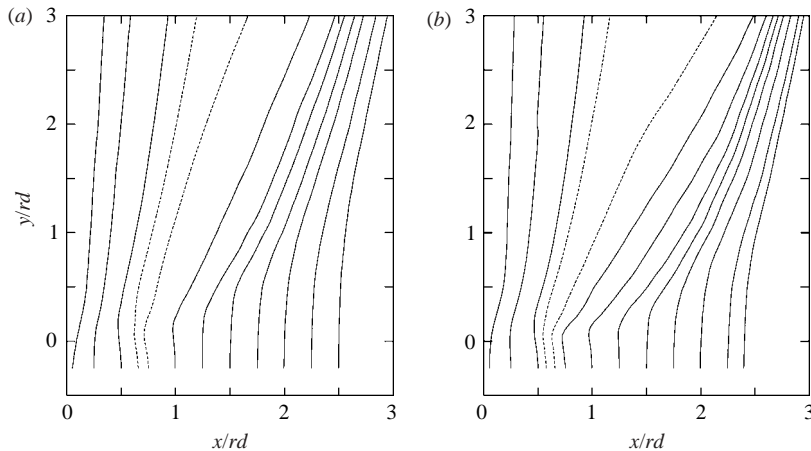


FIGURE 18. Two-dimensional stream traces determined from the mean velocity field results in the  $z = 0.22rd$ , for (a) the protruding nozzle case and (b) the flush nozzle case.

stagnation point, with all streamlines being entrained into the jet. This behaviour has previously been noted by Hasselbrink & Mungal (2001*b*) in crossflowing jets with  $r = 10$  and 21. The patterns for the two nozzle positions do differ in the position of the lee-side stagnation point. For the protruding nozzle case, the stagnation point is located at  $(x, y) \approx (0.25rd, 0.28rd)$ , versus approximately  $(0.15rd, 0.28rd)$  for the flush nozzle case. The absence of a wall in the protruding nozzle case allows considerable entrainment of fluid from upstream of the nozzle exit ( $x < 0$ ), as seen in the streamlines to the  $-x$  side of the stagnation point. This appears to push the stagnation point to the positive  $x$ -direction, relative to its position in the flush nozzle case.

Both streamline patterns in figure 17 also give a good indication of the boundaries of the jet. The outer boundary of the jet is given by the dense cluster of streamlines that follow the trajectory of the centre streamline (the streamline originating from the centre of the nozzle exit,  $(x, y) = (0, 0)$ ). The outer boundary for the protruding nozzle case initially turns more quickly in the crossflow direction than does the outer boundary for the flush nozzle case. At the downstream limit of the measurement area, however, the flow patterns for the two nozzle configurations show similar degrees of penetration into the crossflow, as quantified by their  $x$ -positions. On the windward side of the jet, the inner boundary might be defined as the line separating those streamlines that have an inflection point in turning toward the centre streamline, and those with  $d^2y/dx^2 > 0$ , which do not turn toward the jet. This nominal inner boundary appears to lie between the two dashed streamlines in each of the streamline patterns in figure 17. The inner boundaries are similarly positioned for the two nozzle configurations.

Figure 18 shows the two-dimensional stream trace patterns determined from the mean velocity fields in the  $z = 0.22rd$  plane. For this off-centreplane, these traces (which are computed similarly to those in figures 2*c* and 17) are not true streamlines, because the unmeasured out-of-plane velocity component is not zero. Nevertheless, the lines are everywhere parallel to the local projection of the velocity field onto the  $z = 0.22rd$  plane, and give an indication of the region in the plane from which fluid is entrained into the jet. Consider the dashed stream traces shown in figure 18. For the protruding nozzle case (figure 18*a*), these dashed traces have initial points  $(x, y) = (0.66rd, -0.25rd)$  and  $(0.75rd, -0.25rd)$ , while for the flush nozzle case

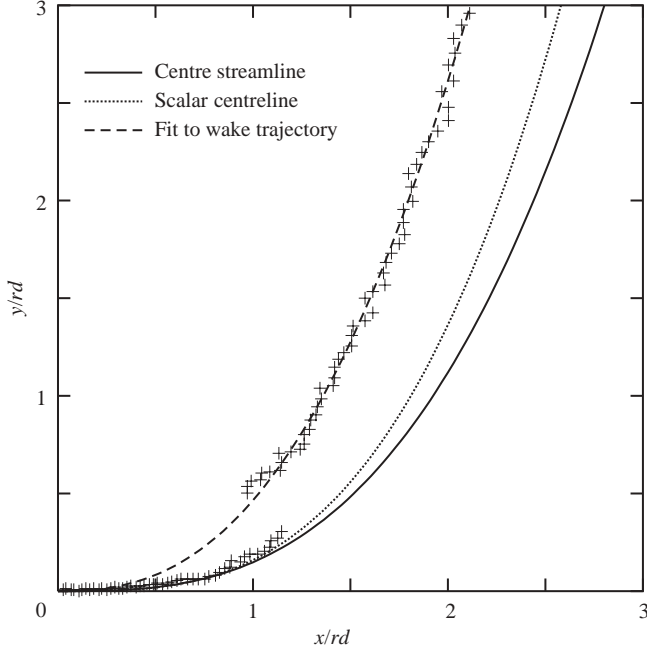


FIGURE 19. The trajectory of the local maxima in the mean crossflow-subtracted velocity magnitude field  $\langle |\mathbf{u} - v_\infty \mathbf{e}_y| \rangle$  in the  $z=0$  plane, together with the scalar centreline (§ 3.1) and centre streamline. Data for the protruding nozzle case.

(figure 18*b*), the initial points are  $(0.58rd, -0.25rd)$  and  $(0.66rd, -0.25rd)$ . The left-hand of the two dashed traces for each of the stream trace patterns has  $d^2y/dx^2 > 0$  uniformly for  $y \gtrsim 0.5rd$ , and is thus not drawn into the jet flow, while the right-hand dashed trace in each pattern shows an inflection point, suggesting entrainment into the jet. However, the dashed traces diverge from each other more rapidly in the flush nozzle case, indicating that the jet in the flush nozzle case affects a significantly larger region of the flow in this  $z = 0.22rd$  plane than does the jet in the protruding nozzle case. This provides additional evidence that the flow for the flush nozzle case spreads more quickly in the out-of-plane  $z$ -direction.

#### 4.2. Flow trajectories

The bifurcated structure of velocity magnitude field in figure 16 is also seen clearly in figure 19, which shows the trajectory of the points of local maximum velocity magnitude in the centreplane, for the protruding nozzle case. Again, the crossflow speed is subtracted from the vertical velocity component. We determine the trajectory of the  $\langle |\mathbf{u} - v_\infty \mathbf{e}_y| \rangle$  field in the same fashion as the scalar trajectories in § 3.1. The centre streamline plotted in the figure is as defined in § 4.1. The points of maximum velocity magnitude initially follow the centre streamline quite closely. In the notation of (3.1), the fit to the centre streamline has  $A = 1.92$  and  $m = 0.342$ . Notably, the centre streamline lies to the windward side of the scalar centreline trajectory. At roughly  $s = 1.3$  (measured along the centre streamline), the points of maximum velocity magnitude abruptly shift to a trajectory lying in the wake region of the flow. The fit to this wake trajectory has  $A = 1.36$  and  $m = 0.402$ . Figure 20 compares the centre streamline and wake trajectories for the protruding and flush nozzle cases, with the

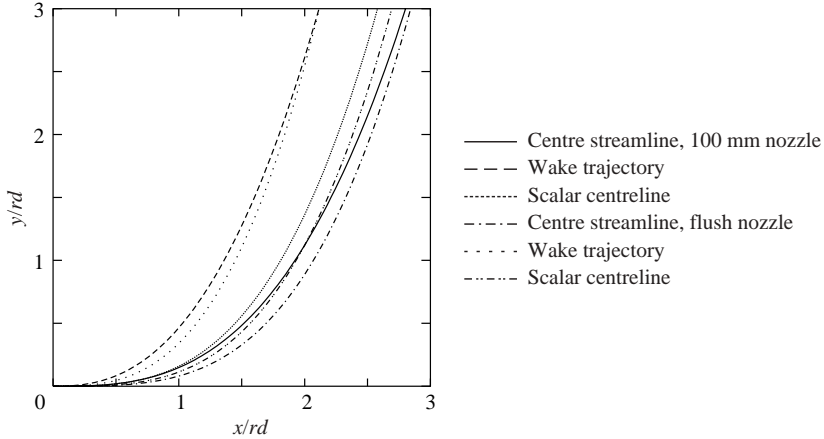


FIGURE 20. Comparison of flow trajectories for both nozzle positions. Shown are the centre streamline, the wake trajectory as described by local maxima in the  $|\mathbf{u} - v_\infty \mathbf{e}_y|$  field, and the scalar centreline.

scalar centrelines shown for comparison. Figure 20 demonstrates again that the flow penetrates further into the crossflow with the nozzle exit placed flush with the facility wall. Whether this trend persists into the far field, however, is somewhat in question. At the upper boundary of the measurement area ( $y \approx 3rd$ ), the wake trajectory for the protruding nozzle case appears to be crossing to the outside of the trajectory for the flush nozzle. Similarly, the centre streamline for the protruding nozzle case draws closer to the centre streamline for the flush case for increasing downstream distance. It is known that the low-pressure region in the wake of the jet has a strong effect on the jet trajectory (e.g. Fric & Roshko 1994; Schlüter *et al.* 1999). It is possible that while the jet issuing from the flush nozzle initially penetrates further into the flow because of the lower crossflow momentum in the boundary layer, the presence of the wall results in a stronger low-pressure region which acts to draw the flow back toward the wall as the flow moves downstream. The streamline patterns of figure 17 provide some support for this, in showing that with the protruding nozzle configuration, there is noticeable entrainment of fluid from the  $x < 0$  region, ‘behind’ the jet nozzle exit. This may relieve the wake pressure deficit somewhat relative to the flush nozzle case, where entrainment from  $x < 0$  is impossible. Clarification of this point may require pressure measurements in the wake region.

#### 4.3. Centreline decay and flow width

As discussed above, the crossflowing jet can be viewed as approximating a pure jet in its near field and a wake in its far field. In attempting to identify these scalings, the choice of appropriate variables is important. For the near field, the jet is described well by the raw velocity magnitude  $|\mathbf{u}|$ . However, because wake scaling is defined in terms of the deficit velocity, the appropriate variable for the crossflowing jet far field is the magnitude of the velocity with the crossflow speed subtracted, as shown in figure 16. In figure 21(a), the decay of the maximum  $\langle |\mathbf{u} - v_\infty \mathbf{e}_y| \rangle$  term is plotted against the downstream coordinate  $s$ , for the flush nozzle case (the protruding nozzle case is qualitatively similar). The two decay curves represent the initial trajectory and later wake trajectory; the curves do not join smoothly because  $s$  is computed separately for each curve based on the individual fits to (3.1). Also plotted in the figure are curves with slope  $-1$  and  $-2/3$ . In the initial portion of the trajectory,

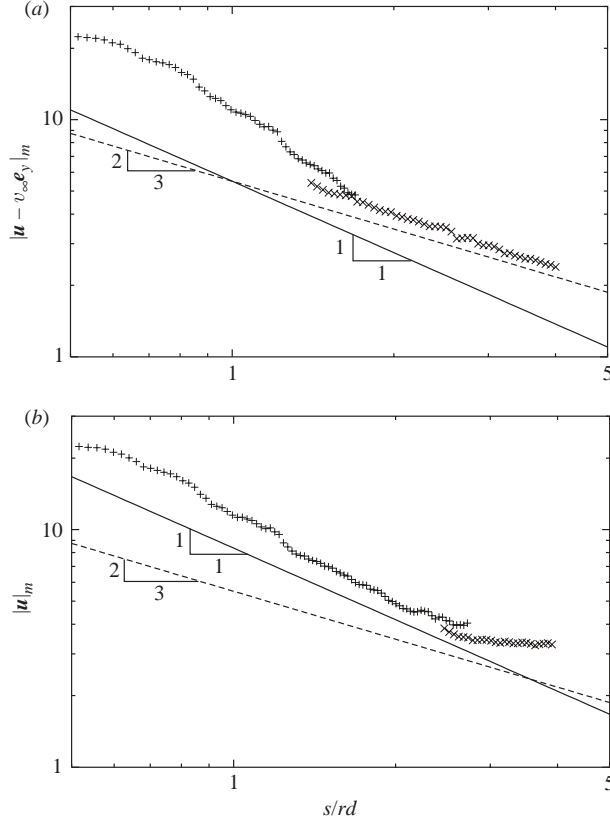


FIGURE 21. Downstream decay of the mean velocity magnitude in the jet centreplane. (a) Decay of the maximum mean crossflow-subtracted velocity magnitude  $|\mathbf{u} - v_\infty \mathbf{e}_y|_m$ , and (b) decay of the maximum mean raw velocity magnitude  $|\mathbf{u}|_m$ . Data for the flush nozzle case.

and outside of the potential core, the magnitude decays faster than  $1/s$ , the pure jet rate, and does not appear to follow a power law scaling. In the wake portion of the trajectory, the magnitude appears to adhere to a power law decay with dependence very close to  $s^{-2/3}$ , suggesting a wake-like scaling. Figure 21(b) shows the maximum mean raw velocity magnitude,  $\langle |\mathbf{u}| \rangle$ , as a function of  $s$ . In this figure, the magnitude along the initial trajectory shows some evidence of following a jet-like decay  $1/s$ , while the magnitude in the wake trajectory shows no power-law dependence, instead asymptotically approaching the crossflow velocity  $v_\infty = 2.95 \text{ m s}^{-1}$ . This emphasizes that the raw velocity magnitude  $|\mathbf{u}|$  is the appropriate variable for revealing the possible jet-like scaling of velocity magnitude decay in the near field, while the crossflow-subtracted magnitude  $|\mathbf{u} - v_\infty \mathbf{e}_y|$  is the proper variable for describing the possible wake-like scaling in the far field.

The flow width of the  $\langle |\mathbf{u} - v_\infty \mathbf{e}_y| \rangle$  field, for both the protruding and flush nozzles, is shown in figure 22. Plotted are the full flow widths  $\delta$ , defined as before as the distance between points, in the trajectory-normal direction, where the magnitude is 20% of the maximum value. (The flow width of the  $\langle |\mathbf{u}| \rangle$  field cannot be determined in this way because the free-stream value of  $\langle |\mathbf{u}| \rangle$  is not zero.) As with the scalar growth rates shown in figure 8, the initial growth rate exceeds the linear dependence of a pure jet. In figure 22, there is then an abrupt transition to a slower growth rate which is very

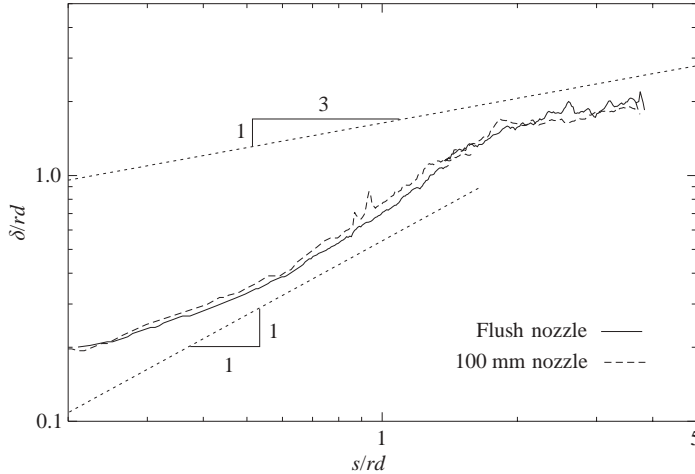


FIGURE 22. Downstream evolution of the full flow width,  $\delta$ , of the  $\langle |\mathbf{u} - v_{\infty} \mathbf{e}_y| \rangle$  field, in the centreplane.

close to the wake growth rate  $s^{1/3}$ . The curves for the flush and protruding nozzle cases are very similar, including the positions of the transition points, again pointing out the similarity in the flow scalings when expressed in terms of  $s$ .

#### 4.4. Three-dimensionality in the velocity field

The results of § 3.3 showed a high degree of three-dimensionality in the mean scalar field, which may explain the failure of the scalar field to observe the expected wake-like centreline scalar concentration decay rate in the far field of the measurement area. In contrast, the velocity field shows wake-like behaviour in both centreline velocity magnitude decay rate and flow width (figures 21 and 22), so we expect three-dimensionality in the mean velocity field to be less marked than in the mean scalar field.

The boundary contours for the  $\langle |\mathbf{u} - v_{\infty} \mathbf{e}_y| \rangle$  field in the centreplane, and in the planes  $z = 0.22rd$ ,  $0.45rd$  and  $0.67rd$ , for the flush nozzle case are shown in figure 23. The boundary contours are defined as in figure 11. Also plotted in figure 23 is the centre streamline. The region enclosed by each contour is heavily weighted toward the  $-x$  side of the centre streamline, indicating the dominance of the wake region in the flow development. The kidney-shaped flow cross-section described by the scalar contours in figure 11 is not duplicated here; instead, the velocity magnitude contours for the planes with higher  $z$  are contained within the contours for lower  $z$ , indicating that the cross-sectional contours of velocity magnitude are everywhere convex in shape. The absence of the out-of-plane velocity component perhaps explains the departure from the kidney-shaped cross-section. (The averaged out-of-plane velocity component in the centreplane of the jet is identically zero by symmetry, and thus its absence does not affect the results shown in figures 19–22.)

Figure 24 gives the profiles of  $\langle |\mathbf{u} - v_{\infty} \mathbf{e}_y| \rangle$  in the  $z$ -direction, for  $s = 1.5rd$ ,  $2.0rd$ ,  $3.0rd$  and  $4.0rd$  and  $n = 0$ . The data are for the flush nozzle case. The  $s$ -coordinate used in figure 24 is that determined from the least-squares fit to the wake trajectory, as defined in § 4.2, ensuring that the velocity magnitude values at  $z = 0$  in the profiles represent the local maxima. The figure shows that the maximum velocity magnitude lies on the centreline for each of the given downstream positions. There is some

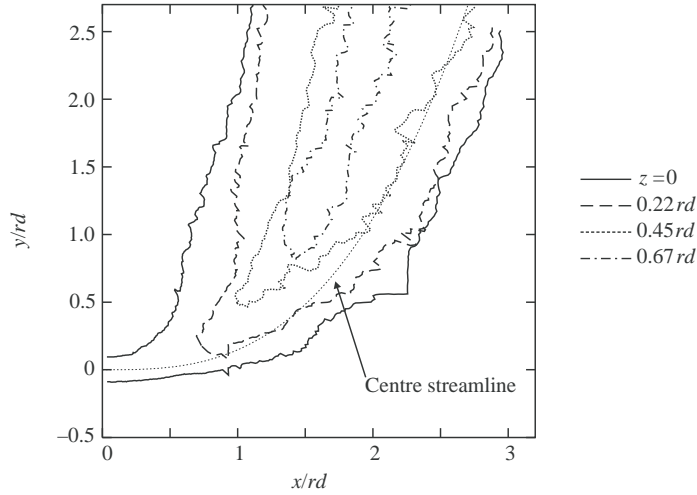


FIGURE 23. Boundary contours for the  $\langle |\mathbf{u} - v_\infty \mathbf{e}_y| \rangle$  field. Data for the flush nozzle case.

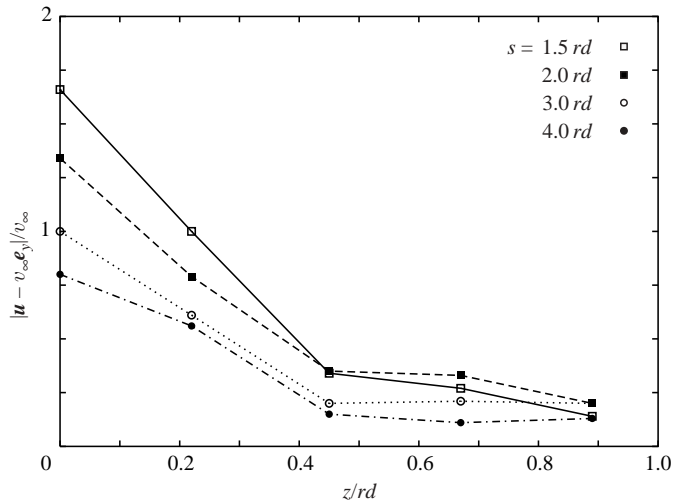


FIGURE 24. Profiles of mean crossflow-subtracted velocity magnitude,  $\langle |\mathbf{u} - v_\infty \mathbf{e}_y| \rangle$ , in the out-of-plane  $z$ -direction, for  $s = 1.5rd$ ,  $2.0rd$ ,  $3.0rd$  and  $4.0rd$  and  $n = 0$ . The  $s$ -coordinate is defined along the velocity magnitude centreline. Data for the flush nozzle case.

uncertainty in this conclusion, given the highly discrete nature of these  $z$ -profiles; even so, there is no indication that the form of the profiles changes with increasing  $s$  to a bimodal profile, as do the scalar field profiles (figure 10). In particular, the  $z$ -profiles of  $\langle |\mathbf{u} - v_\infty \mathbf{e}_y| \rangle$  are much nearer to observing self-similarity than are the scalar field profiles.

Figure 25 presents profiles of  $\langle |\mathbf{u} - v_\infty \mathbf{e}_y| \rangle$  along the trajectory-normal direction,  $n$ , in the different  $z$ -planes, for  $s = 2.0rd$ ,  $3.0rd$  and  $4.0rd$ . The downstream coordinate,  $s$ , used here is measured along the centre streamline. These profiles differ from the corresponding scalar profiles (figure 12) in that the maximum velocity magnitude values lie in the centreplane, as also noted in figure 24. The velocity magnitude

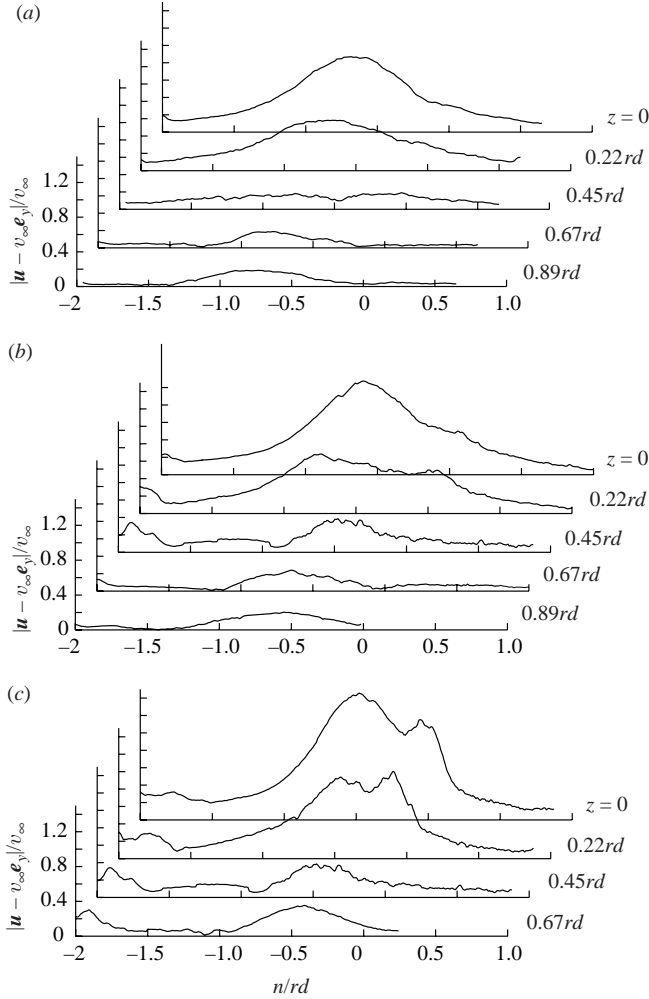


FIGURE 25. Profiles of mean crossflow-subtracted velocity magnitude,  $\langle |\mathbf{u} - v_\infty \mathbf{e}_y| \rangle$ , along the trajectory-normal coordinate,  $n$ , in the different  $z = \text{const}$  measurement planes, for (a)  $s = 4.0rd$ , (b)  $s = 3.0rd$  and (c)  $s = 2.0rd$ .

profiles in the  $z = 0$  plane are also more symmetric than the scalar profiles for  $z = 0$ . In fact, at  $s = 4.0rd$ , the profiles for  $z = 0$  and  $0.22rd$  are both near-symmetric, and have maxima at nearly equal  $n$  values. This is again consistent with a more self-similar evolution in the velocity field than in the scalar field.

#### 4.5. Mean velocity field $x$ - and $y$ -profiles

Figure 26 presents profiles of the averaged velocity magnitude in the centreplane, along lines of fixed  $x$  and fixed  $y$ . The profiles are computed as were the scalar field profiles in §3.4. As recommended by figure 21, the more upstream profiles (those for fixed  $x$ ) are compiled for the averaged raw velocity magnitude,  $\langle |\mathbf{u}| \rangle$ , while the more downstream, fixed- $y$  profiles are compiled for the crossflow-subtracted magnitude,  $\langle |\mathbf{u} - v_\infty \mathbf{e}_y| \rangle$ . The forms of the  $\langle |\mathbf{u}| \rangle$  profiles in the near field are similar to the mean scalar field profiles of figure 13. In particular, the  $x = 0.1rd$ ,  $0.5rd$  and  $1.0rd$  profiles show a bell-shaped peak coinciding roughly with the centre streamline, and

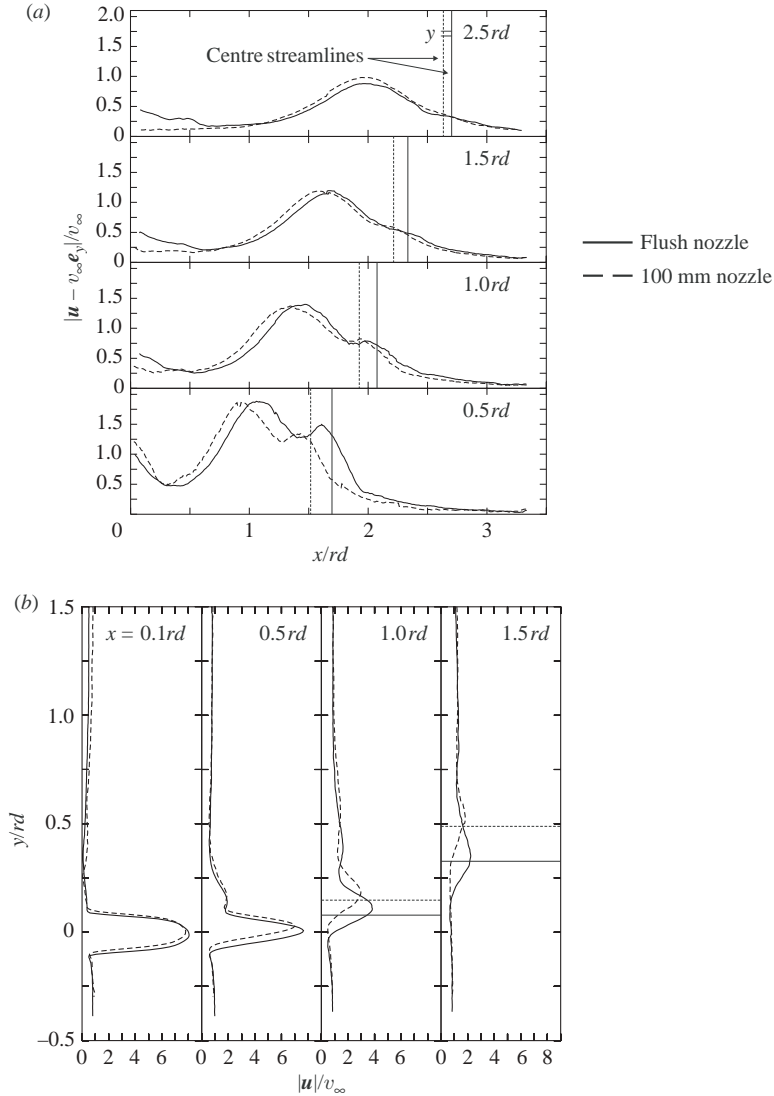


FIGURE 26. Averaged velocity magnitude profiles in the jet centreplane, for both the flush and protruding nozzle cases. (a) The profiles of the averaged crossflow-subtracted velocity magnitude,  $\langle |\mathbf{u} - v_\infty \mathbf{e}_y| \rangle$ , for  $y = 0.5rd, 1.0rd, 1.5rd$  and  $2.5rd$ , and (b) the profiles of the averaged raw velocity magnitude,  $\langle |\mathbf{u}| \rangle$ , for  $x = 0.1rd, 0.5rd, 1.0rd$  and  $1.5rd$ .

depart from symmetry through the presence of elevated  $\mathbf{u}$  values in the wake region (positive  $y$ ).

The profiles of  $\langle |\mathbf{u} - v_\infty \mathbf{e}_y| \rangle$  for  $y = 0.5rd$  and  $1.0rd$  depart noticeably from the corresponding scalar field profiles in figure 13 in showing two distinct peaks, with one near the position of the centre streamline, and with the other, stronger peak lying in the wake region. As the flow evolves downstream, the peak near the centre streamline weakens, largely disappearing by  $y = 2.5rd$ . The resulting profile is nearly symmetric, centred about the peak in the wake region. This again differs from the scalar field profiles, which were centred near the centre streamlines; the velocity

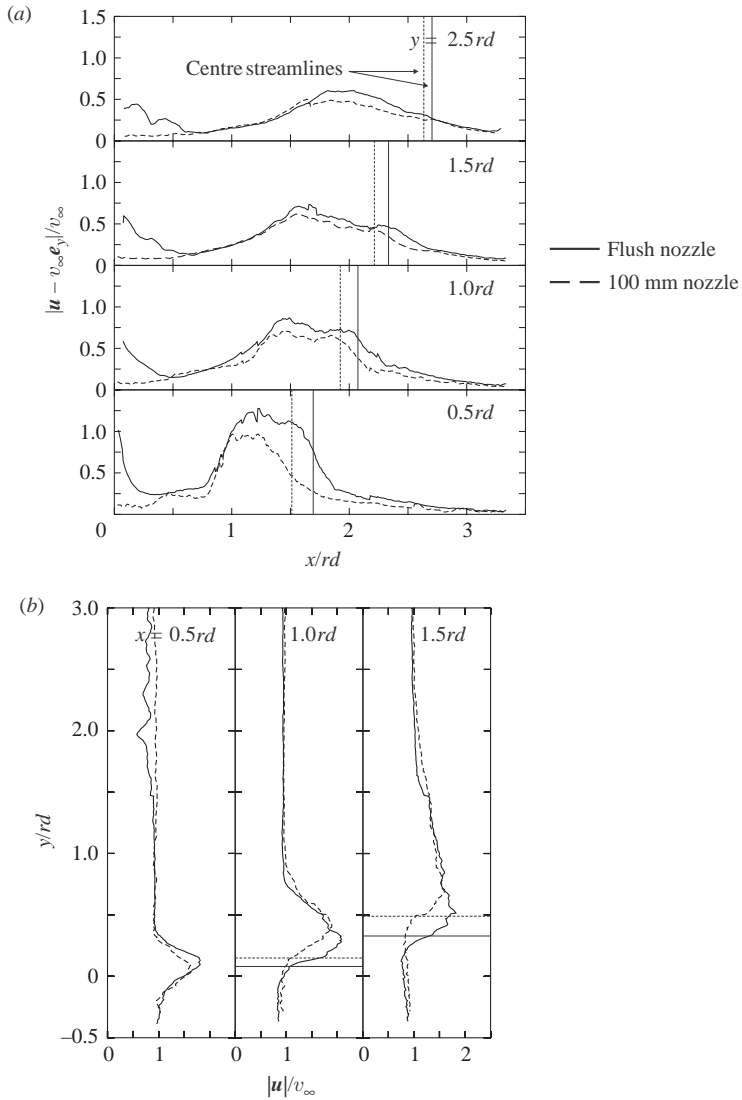


FIGURE 27. Averaged velocity magnitude profiles in the  $z=0.22rd$  plane, for both the flush and protruding nozzle cases. (a) The profiles of  $\langle |\mathbf{u} - v_\infty \mathbf{e}_y| \rangle$  for  $y=0.5rd$ ,  $1.0rd$ ,  $1.5rd$  and  $2.5rd$  and (b) the profiles of  $\langle |\mathbf{u}| \rangle$  for  $x=0.5rd$ ,  $1.0rd$  and  $1.5rd$ .

magnitude profiles at these far downstream positions also appear more symmetric (save for the evidence of the boundary layer in the flush nozzle case) than do the scalar field profiles.

The averaged velocity magnitude profiles in the  $z=0.22rd$  and  $0.45rd$  planes are given in figures 27 and 28, respectively. The profiles in the  $z=0.22rd$  plane are qualitatively similar to these in the centreplane. Evidence of the bimodal profile structure remains in the  $y=1.0rd$  and  $1.5rd$  profiles, with the  $y=2.5rd$  profiles approaching symmetry around a single wake-side peak. Unlike the scalar field profiles in the  $z=0.22rd$  plane (figure 14), the velocity magnitudes in the  $z=0.22rd$  plane are everywhere lower than the corresponding magnitudes in the centreplane. In the

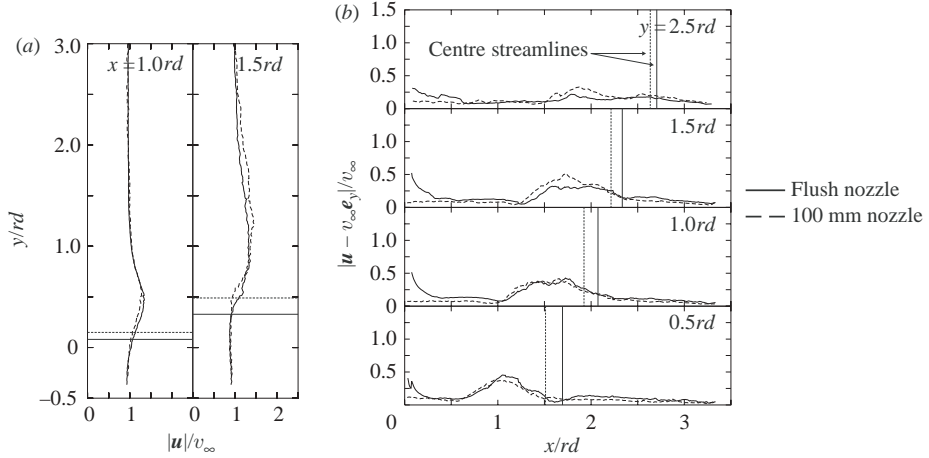


FIGURE 28. Averaged velocity magnitude profiles in the  $z = 0.45rd$  plane, for both the flush and protruding nozzle cases. (a) The profiles of  $\langle |\mathbf{u}| \rangle$  for  $x = 1.0rd$  and  $1.5rd$ , and (b) the profiles of  $\langle |\mathbf{u} - v_\infty \mathbf{e}_y| \rangle$  for  $y = 0.5rd, 1.0rd, 1.5rd$  and  $2.5rd$ .

$z = 0.45rd$  plane, the bimodal form of the fixed- $y$  velocity magnitude profiles no longer pertains, with only the peak in the wake region being evident. Interpretation of the profiles in the  $z = 0.45rd$  plane is, however, constrained somewhat by limited statistical convergence.

Finally, as with the scalar field profiles, the velocity magnitude profiles for the flush and protruding nozzle configurations are in good agreement (excepting the boundary layer evident in the flush nozzle case) at  $y = 2.5rd$ , for the different  $z$ -planes shown. This further supports the idea that the asymptotic state of the flow is independent of the nozzle position.

## 5. Turbulence quantities

Turbulence quantities involving the fluctuating velocity and scalar field terms are available owing to the high resolution of the present data. In particular, the simultaneous nature of the measurements permits the scalar flux components,  $\langle u'C' \rangle$  and  $\langle v'C' \rangle$ , to be determined. These represent unresolved terms in the Reynolds-averaged scalar transport equation, and correspond to subgrid production terms in LES-filtered scalar transport. From the evidence of previous computations, these scalar flux terms are very difficult to compute accurately (Alvarez *et al.* 1993). This section also presents results for the scalar variance,  $C'^2$ , and the  $u'^2$ ,  $v'^2$  and  $u'v'$  components of the turbulent stress tensor.

### 5.1. Resolution estimates

The accuracy of the measured fluctuation quantities is dependent upon the resolution of the data. Following Su & Clemens (2003), we write

$$\lambda_v = \Lambda \delta Re_\delta^{-3/4}. \quad (5.1)$$

Here,  $\lambda_v$  represents the characteristic full width of a structure in the kinetic energy

$s/rd$	$U$ (m/s)	$\delta$ (m)	$Re_\delta$	$\lambda_v$ ( $\mu\text{m}$ )	$\lambda_D$ ( $\mu\text{m}$ )	$\Delta x_C$ ( $\mu\text{m}$ )	$\Delta x_u$ ( $\mu\text{m}$ )
1	11.3	0.019	14100	220	180	175	230
2	4.0	0.041	10800	580	480	175	310
3	3.0	0.046	9100	740	610	175	420
3.5	2.6	0.052	8900	850	700	175	420

TABLE 3. Outer scale parameters and resolution estimates. The estimated finest length scales in the velocity and scalar fields are given by  $\lambda_v$  and  $\lambda_D$ , respectively. The grid resolution of the scalar field images is  $\Delta x_C$ , and the grid resolution of the velocity fields is given by  $\Delta x_u$ .

dissipation rate fields,  $\delta$  is a measure of the local mean flow width, and the local outer scale Reynolds number,  $Re_\delta$ , is defined in terms of  $\delta$  and a velocity  $U$  quantifying the mean shear. Defining the flow width  $\delta$  as the distance between the 20% points of the velocity magnitude profile, Su & Clemens (2003) suggest a value for the proportionality constant  $\Lambda \approx 15$ . For the scalar mixing, the characteristic full width of a structure in the scalar energy dissipation rate field is given by

$$\lambda_D = \lambda_v Sc^{-1/2}, \quad (5.2)$$

where the Schmidt number,  $Sc$ , for this flow system is 1.49 (§2).

To determine  $\lambda_v$  and  $\lambda_D$  for various downstream positions  $s$  in the present data, we estimate  $\delta$  from figure 22 and  $U$  from figure 21. These outer scale parameters, and the resulting outer scale Reynolds number  $Re_\delta$ , are given in table 3 for  $s/rd = 1, 2, 3$  and 3.5. Table 3 also presents the resolution estimates determined from (5.1) and (5.2).

The downstream positions  $s$  shown are those determined from the wake portion of the velocity magnitude trajectory shown in figure 19. For  $s/rd = 1$ , the flow still follows the initial trajectory (see, for example, figure 19 or 22), so the relevant  $U$  is the maximum mean raw velocity magnitude,  $|\mathbf{u}|_m$  (figure 21a), and the proper  $\delta$  is the flow width of the  $\langle |\mathbf{u}| \rangle$  field (not shown). For  $s/rd = 2, 3$  and 3.5, the flow follows the wake trajectory, so the proper  $U$  is the maximum mean crossflow-subtracted velocity magnitude  $|\mathbf{u} - v_\infty \mathbf{e}_y|_m$  (figure 21b), with flow width  $\delta$  from figure 22. The resulting length scale estimates  $\lambda_v$  and  $\lambda_D$  are found from (5.1) and (5.2) using a proportionality constant  $\Lambda = 15$ . The grid spacing in the scalar field data is  $\Delta x_C = 175.1 \mu\text{m}$ , which resolves the scale  $\lambda_D$  at all positions shown, with Nyquist resolution except at  $s/rd = 1$ . The grid spacing in the velocity fields,  $\Delta x_u$ , slightly exceeds  $\lambda_v$  at  $s/rd = 1$ , but easily resolves  $\lambda_v$  for the remaining positions. ( $\Delta x_u$  varies because of the different sizes of the PIV imaging windows, shown in figure 2.) These are rough estimates; the question of the true  $U$  and  $\delta$  characterizing the outer scales of the developing region of the crossflowing jet is an open one.

## 5.2. Scalar variance

Figure 29 shows the averaged scalar variance fields,  $\langle C'^2 \rangle$ , for the flush nozzle case, in the centreplane and the planes  $z = 0.22rd, 0.45rd$  and  $0.67rd$ . The fields for  $z \leq 0.45rd$  show local maxima both on the jet outer boundary and in the jet wake region. This bifurcated structure is familiar from mixing in canonical shear flows, such as mixing layers or jets, with the peak variances being associated with steep gradients in the mean scalar fields. Sherif & Pletcher (1991) previously observed the bifurcated structure of the scalar variance in crossflowing jets. The averaged  $\langle C'^2 \rangle$

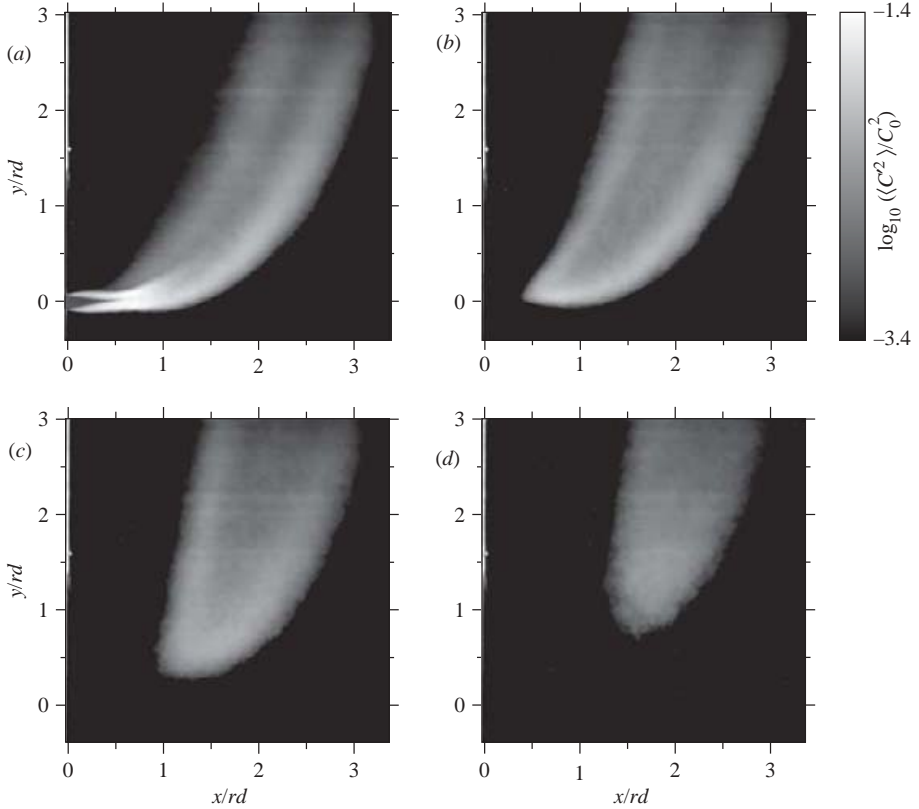


FIGURE 29. Averaged scalar variances,  $\langle C'^2 \rangle$ , for the flush nozzle case, in the planes (a)  $z=0$ , (b)  $z=0.22rd$ , (c)  $z=0.45rd$ , and (d)  $z=0.67rd$ .

field at  $z=0.67rd$  (figure 29d) shows less evidence of a bifurcation, probably owing to the proximity of this plane to the jet boundary in the  $z$ -direction.

A more quantitative view is available by considering profiles of  $\langle C'^2 \rangle$ . Figure 30 presents  $x$ - and  $y$ -profiles of  $\langle C'^2 \rangle$  in the  $z=0$  plane for both the flush and protruding nozzle cases. In the jet near field, at  $x=0.1rd$  and  $x=0.5rd$ , the profiles are approximately symmetric about the centreline, and the discrepancy between the two nozzle configurations is small. Just outside of the potential core, at  $x=1.0rd$ , the bifurcated structure of the variance profile is distinctly asymmetric, with the windward peak being much stronger than the wake-side peak; additionally, the variances are noticeably higher for the flush nozzle than for the protruding nozzle configuration. These trends persist as the jet turns in the crossflow direction, as seen in the  $x=1.5rd$ ,  $y=0.5rd$  and  $y=1.0rd$  profiles. Both the profile asymmetry and the discrepancy between nozzle configurations are most significant at  $y=0.5rd$ . By  $y=1.5rd$ , the two nozzle configurations show similar profile magnitudes, while at  $y=2.5rd$ , the variance profiles are again nearly symmetric, with symmetry axes to the wake side of the centre streamline.

The variance profiles in the off-centreplanes suggest, however, that the asymptotic downstream state of the scalar variance is not characterized by symmetry between the windward and wake sides of the flow. Figure 31 and 32 show the profiles of  $\langle C'^2 \rangle$  in the  $z=0.22rd$  and  $0.45rd$  planes, respectively. In both of these planes, the variance

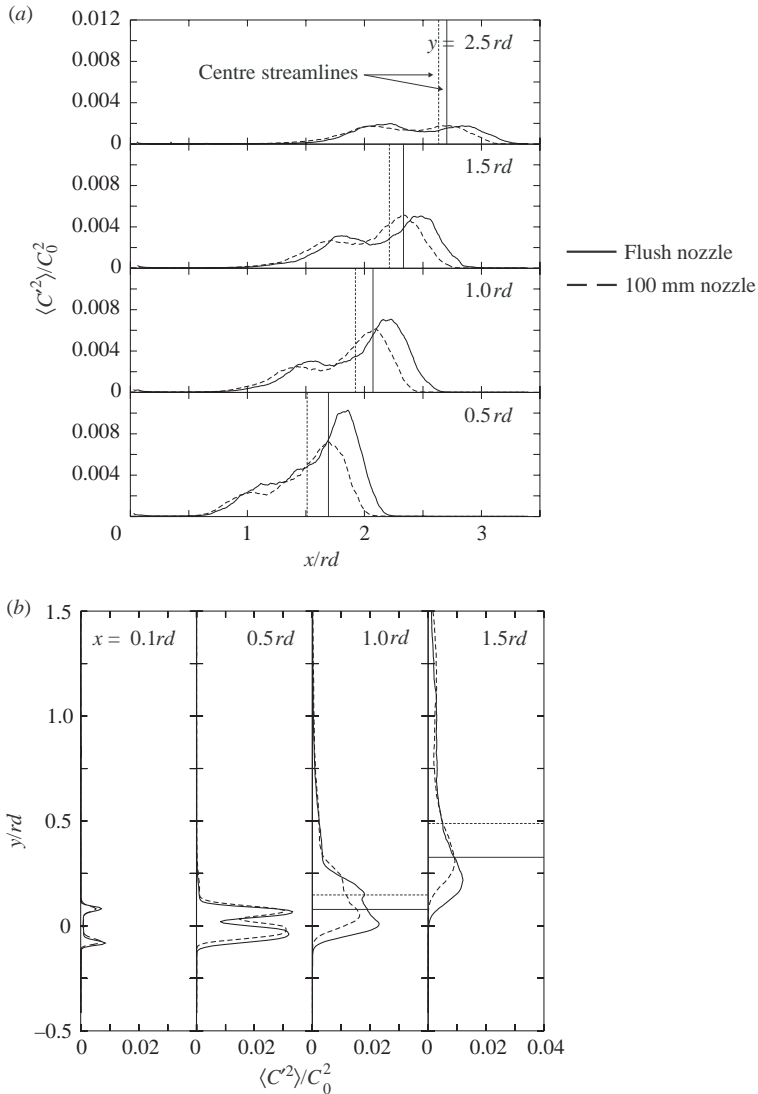


FIGURE 30. Averaged scalar variance profiles in the jet centreplane, for both the flush and protruding nozzle cases. (a) The profiles for  $y = 0.5rd, 1.0rd, 1.5rd$  and  $2.5rd$  and (b) the profiles for  $x = 0.1rd, 0.5rd, 1.0rd$  and  $1.5rd$ .

profiles (for both nozzle configurations) observe similar trends to those seen in the  $z = 0$  plane, except that the wake-side variance peak is larger than the windward-side peak at large  $y$  values. This can be seen in the  $y = 2.5rd$  profile in the  $z = 0.22rd$  plane, and in the  $y = 1.5rd$  and  $2.5rd$  profiles in the  $z = 0.45rd$  plane. The implication of this is that as the flow moves downstream, there is more pronounced mixing between jet and ambient fluid on the wake side of the flow than on the windward side, possibly due to the persistence of the coherent vortical structures in the wake region (e.g. Kelso *et al.* 1996). This asymmetry in the variance profiles is inconsistent with the assumption of wake-like asymptotic similarity in the mixing field, and further contributes to the failure of the scalar field to observe wake scaling with increasing downstream distance (§ 3.2).

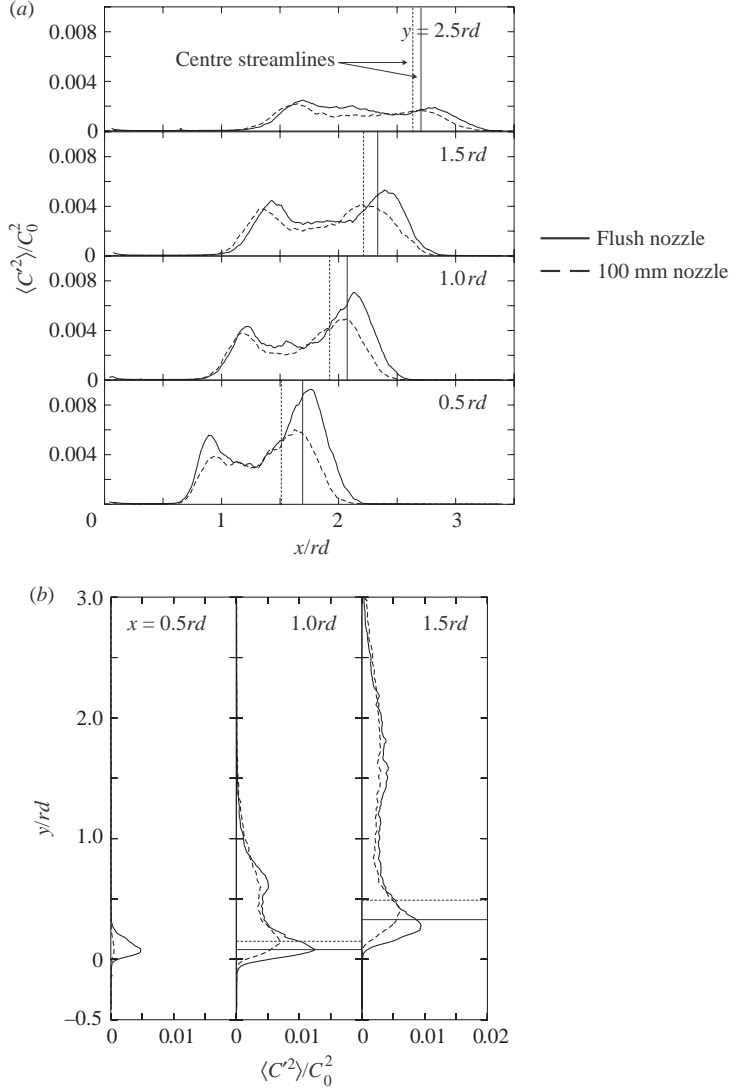


FIGURE 31. Averaged scalar variance profiles in the  $z = 0.22rd$  plane, for both the flush and protruding nozzle cases. (a) The profiles for  $y = 0.5rd, 1.0rd, 1.5rd$  and  $2.5rd$  and (b) the profiles for  $x = 0.5rd, 1.0rd$  and  $1.5rd$ .

### 5.3. Turbulent scalar flux profiles

The turbulent scalar flux terms, defined as the product of the scalar fluctuation term and the components of the velocity fluctuations,  $u'_i C'$ , appear in the Reynolds-averaged scalar transport equation (here in non-dimensional form):

$$\langle u_i \rangle \frac{\partial \langle C \rangle}{\partial x_i} - \frac{1}{Re Sc} \frac{\partial^2}{\partial x_i \partial x_i} \langle C \rangle = - \frac{\partial}{\partial x_i} \langle u'_i C' \rangle, \quad (5.3)$$

where  $Re$  is the Reynolds number formed from the length and velocity scales used for normalization, and  $Sc$  is the Schmidt number. The scalar fluxes,  $\langle u'_i C' \rangle$ , are unresolved in a RANS simulation, and must be modelled to close (5.3). (In the context of large-eddy simulation, where quantities are decomposed into filtered (denoted by  $\overline{(\ )}$ ) and

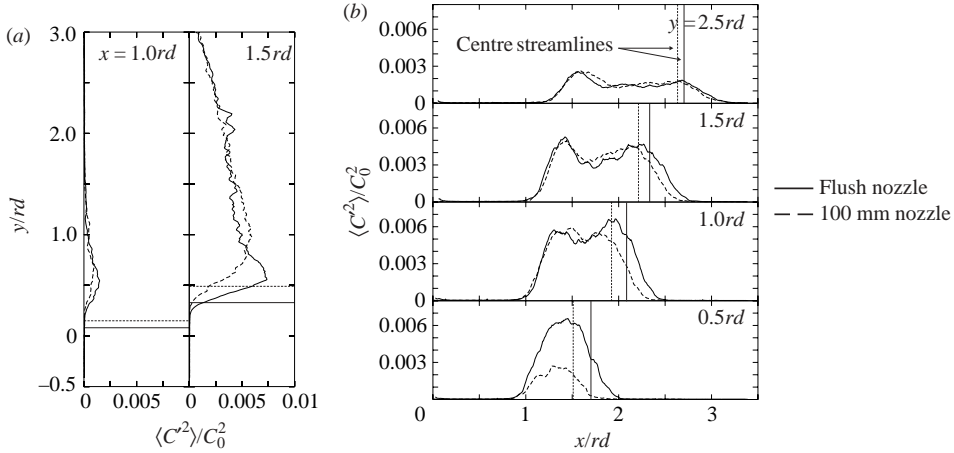


FIGURE 32. Averaged scalar variance profiles in the  $z = 0.45rd$  plane, for both the flush and protruding nozzle cases. (a) The profiles for  $x = 1.0rd$  and  $1.5rd$  and (b) the profiles for  $y = 0.5rd, 1.0rd, 1.5rd$  and  $2.5rd$ .

subgrid (denoted by  $\prime\prime$ ) parts, the divergence of the corresponding filtered LES scalar flux vector,  $\overline{u_i'' C''}$ , appears in the production term for the filtered scalar field,  $\overline{C}$ . In the LES of mixing, these scalar fluxes are also unresolved and are thus entrusted to subgrid models.)

Figure 33 shows profiles of the scalar flux components  $\langle u' C' \rangle$  and  $\langle v' C' \rangle$ , in the centreplane for the flush nozzle case. The same profiles for the protruding nozzle configuration are shown in figure 34. The profiles indicate that  $\langle u' C' \rangle$  and  $\langle v' C' \rangle$  are negatively correlated throughout the measurement area. Beyond the potential core, on the windward side of the jet,  $\langle u' C' \rangle$  is positive, with the peak positive value occurring slightly outside the jet centre streamline, and  $\langle v' C' \rangle$  is negative. On the lee side,  $\langle u' C' \rangle < 0$  and  $\langle v' C' \rangle > 0$ . The location at which the signs of these terms change lies slightly to the wake side of the centre streamline. The profiles for the flush and protruding nozzle cases differ in that the peak values of  $\langle u_i' C' \rangle$  are slightly higher for the flush case, in the near field. Toward the downstream side of the measurement area (specifically,  $y \geq 1.0rd$ ), the magnitudes of  $\langle u_i' C' \rangle$  are similar for both nozzle configurations.

The form of the  $\langle v' C' \rangle$  profile, in particular, seems counterintuitive. A simple interpretation of this term might hold that since the crossflowing jet imposes a deficit velocity in the  $y$ -direction, fluid elements originating in the crossflow will have a  $v$ -component of velocity in excess of the mean ( $v' > 0$ ), while having scalar concentration less than the mean ( $C' < 0$ ). Then  $\langle v' C' \rangle$  would be uniformly negative, which is not the form of  $\langle v' C' \rangle$  measured here. Instead, both the  $\langle v' C' \rangle$  and  $\langle u' C' \rangle$  profiles can be readily interpreted in terms of the spread and centreline concentration decay of the jet. To interpret the  $\langle v' C' \rangle$  term, we see from, for example, figure 11 that turbulent advection into the jet is marked by  $v' > 0$  on the jet outer boundary, and  $v' < 0$  on the inner boundary. As a result, negative  $\langle v' C' \rangle$  values to the outside of the jet, and positive values to the inside, show that fluid elements advected in the  $y$ -direction towards the centre of the jet are characterized by excess ambient fluid concentration ( $C' < 0$ ). Positive values of  $\langle u' C' \rangle$  to the outside (increasing  $x$ ) of the jet, and negative  $\langle u' C' \rangle$  to the inside, indicate that fluid elements undergoing turbulent advection in

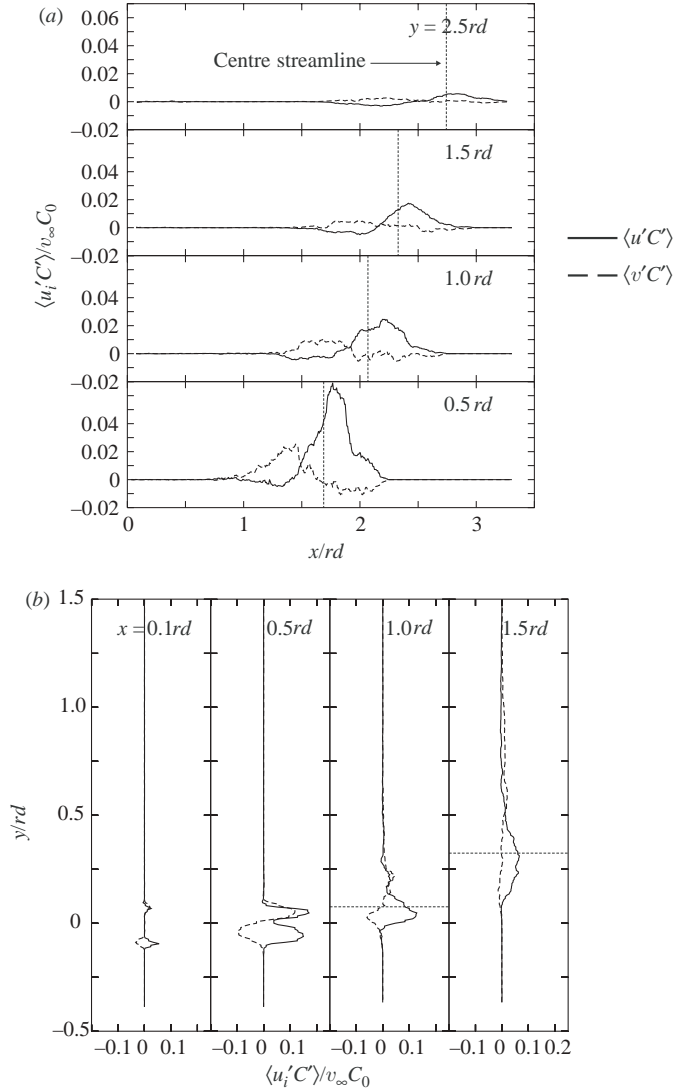


FIGURE 33. Scalar flux profiles in the jet centreplane, for the flush nozzle case. (a) The profiles of  $\langle u' C' \rangle$  and  $\langle v' C' \rangle$  for  $x = 0.1rd, 0.5rd, 1.0rd$  and  $1.5rd$  and (b) the profiles for  $y = 0.5rd, 1.0rd, 1.5rd$  and  $2.5rd$ .

the  $x$ -direction towards the boundaries of the jet (i.e. on the outer part of the jet,  $u' > 0$ , and on the inner part,  $u' < 0$ ) are characterized by excess jet fluid concentration ( $C' > 0$ ). The measured  $\langle u_i' C' \rangle$  thus reflect the spread of the jet boundaries, and the decay of maximum scalar concentration, with increasing downstream distance.

The present data are consistent with the heat flux profiles reported by Andreopoulos (1983), in showing a negative correlation between  $\langle u' C' \rangle$  and  $\langle v' C' \rangle$ , although that earlier study does not show sign changes in the profiles. Instead, the  $\langle u_i' C' \rangle$  profiles of Andreopoulos resemble the portion of the profiles of figures 33 and 34 for the outer part of the jet, with  $\langle u' C' \rangle > 0$  and  $\langle v' C' \rangle < 0$ . The data of Andreopoulos are for a jet with nozzle exit flush with a wall, and with very low velocity ratio,  $r = 0.5$ ; with that

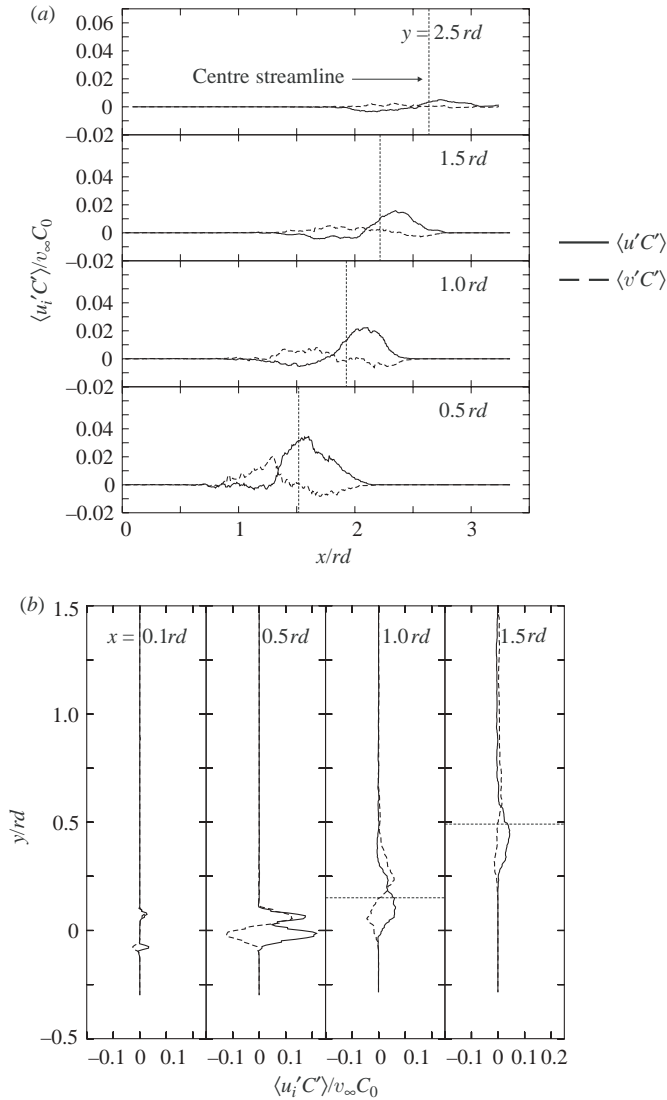


FIGURE 34. Scalar flux profiles in the jet centreplane, for the protruding nozzle case. (a) The profiles of  $\langle u' C' \rangle$  and  $\langle v' C' \rangle$  for  $y = 0.5rd, 1.0rd, 1.5rd$  and  $2.5rd$  and (b) the profiles for  $x = 0.1rd, 0.5rd, 1.0rd$  and  $1.5rd$ .

configuration, the lee side of the jet impinges on the wall. The  $r = 0.5$  jet thus has no free inner (lee-side) boundary, which explains why the  $\langle u_i' C' \rangle$  profiles for the  $r = 0.5$  flow agree only with the windward portion of the profiles for the  $r = 5.7$  flow.

In the large-eddy simulations by Yuan (1997) of  $r = 3.3$  scalar mixing, in which the jet nozzle exit is also flush with a wall, the profiles of mean scalar concentration show that the jet stands clear of the wall, with a distinct inner boundary in the mixing field. Accordingly, the  $\langle u' C' \rangle$  profiles show sign changes similar to those for the present  $r = 5.7$  jet. The work of both Andreopoulos (1983) and Yuan (1997) suggests that the transitional value of  $r$ , above which the jet inner boundary is free of the wall and the  $\langle u_i' C' \rangle$  profiles resemble those of figures 33 and 34, is between 1.0 and 2.0.

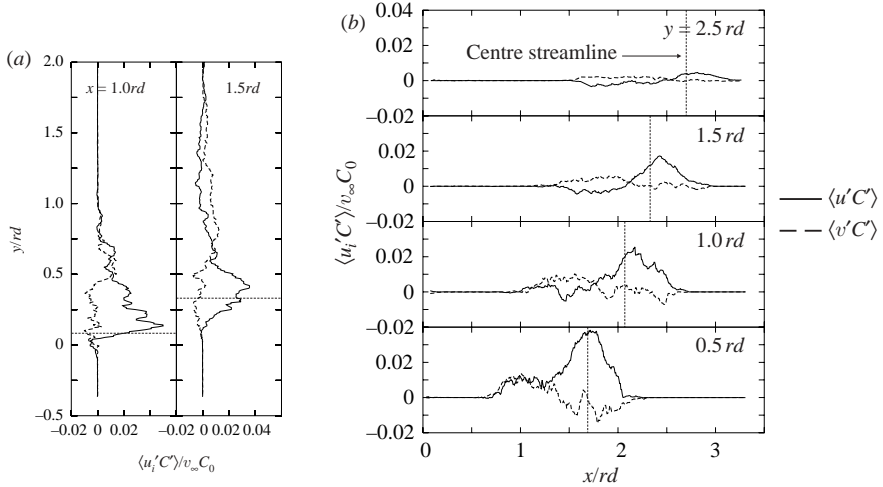


FIGURE 35. Scalar flux profiles in the  $z = 0.22rd$  plane, for the flush nozzle case. (a) The profiles of  $\langle u' C' \rangle$  and  $\langle v' C' \rangle$  for  $x = 1.0rd$  and  $1.5rd$  and (b) the profiles for  $y = 0.5rd, 1.0rd, 1.5rd$  and  $2.5rd$ .

It is also instructive to compare the magnitudes of the  $\langle u' C' \rangle$  and  $\langle v' C' \rangle$  profiles in figures 33 and 34. The  $\langle u' C' \rangle$  component consistently has a higher magnitude than the  $\langle v' C' \rangle$  component, suggesting that in the centreplane, turbulent scalar transport in the cross-stream direction is more significant than transport in the streamwise direction. Also, the highest magnitudes of  $\langle u' C' \rangle$  are on the outer portion of the jet, indicative of stronger turbulent scalar transport on the windward side, though the discrepancy between  $|\langle u' C' \rangle|$  on the windward and wake sides of the jet weakens with increasing downstream distance. This is consistent with the  $\langle C^2 \rangle$  results of § 5.2, which showed higher scalar variance values on the windward side, with the values on the windward and wake sides approaching equality at the downstream limit of the imaging region. Yuan (1997) observed also that the near-field discrepancy in  $|\langle u' C' \rangle|$  on the windward and wake sides decreased as the jet Reynolds number increased.

Figures 35 and 36 show the profiles of  $\langle u_i' C' \rangle$  for the flush nozzle case in the  $z = 0.22rd$  and  $0.45rd$  planes, respectively. (The data for the protruding nozzle case are qualitatively similar.) In the  $z = 0.22rd$  plane, the primary difference with the results for the centreplane is that  $\langle u' C' \rangle > 0$  on the wake side of the jet for  $y = 0.5rd$  (this is also weakly evident for  $y = 1.0rd$ ). In the  $z = 0.45rd$  plane, though the trends are obscured by the limited statistical convergence of the measurements, traceable to the smaller number of images collected, it appears that  $\langle u' C' \rangle > 0$  for  $y \geq 0.5rd$ . Yuan (1997) proposed that positive values of  $\langle u' C' \rangle$  in the off-centreplanes reflected the probability that fluid parcels with excess velocity in the initial jet momentum direction would also have excess jet fluid concentration.

This interpretation can also be cast in terms of the large-scale organization of the velocity field. At the edges of jet in the  $z$ -direction, the  $x$ -component of the crossflow fluid velocity relative to the jet fluid velocity is negative, as the crossflow fluid is diverted around the jet into the wake region (this also agrees with the sense of rotation of the counter-rotating vortex pair). Then  $u' < 0$  correlates with  $C' < 0$  (crossflow fluid), so  $\langle u' C' \rangle > 0$ . This picture is also consistent with the negative values of  $\langle u' C' \rangle$  observed on the wake side of the flow in the centreplane, and in the  $z = 0.22rd$  plane for  $y \geq 1.5rd$ . The CVP is associated with the positive  $x$ -component

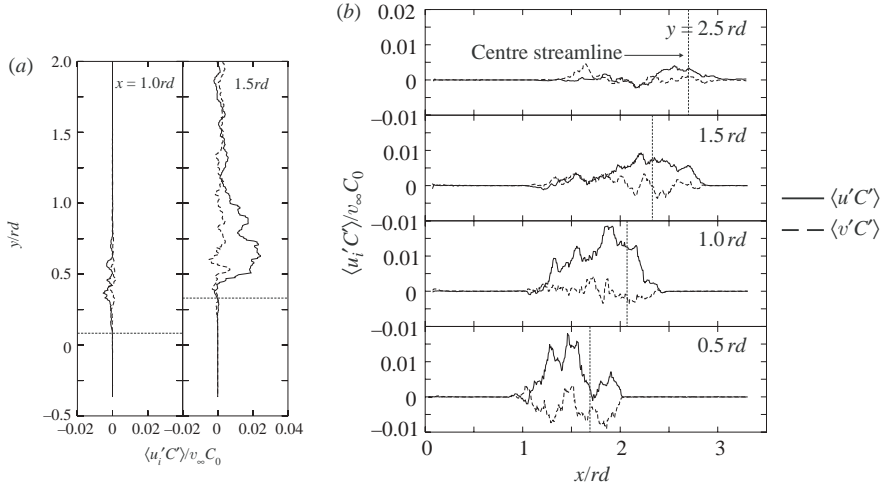


FIGURE 36. Scalar flux profiles in the  $z = 0.45rd$  plane, for the flush nozzle case. (a) The profiles of  $\langle u'C' \rangle$  and  $\langle v'C' \rangle$  for  $x = 1.0rd$  and  $1.5rd$  and (b) the profiles for  $y = 0.5rd, 1.0rd, 1.5rd$  and  $2.5rd$ .

of velocity on the wake side in the centreplane, but, as seen in the streamline patterns of figure 17, those fluid parcels with  $u' > 0$  carry crossflow fluid ( $C' < 0$ ) into the jet, giving  $\langle u'C' \rangle < 0$ .

#### 5.4. Turbulent stresses

Figure 37 shows profiles of the in-plane turbulent normal stress components (equivalently, components of the turbulent kinetic energy),  $\langle u'^2 \rangle$  and  $\langle v'^2 \rangle$ , and the turbulent shear stress,  $\langle u'v' \rangle$ , for the centreplane for the flush nozzle case. Figure 38 gives profiles of the same quantities for the centreplane in the protruding nozzle case. The results for the flush and protruding nozzle positions are very similar, the primary difference being the slightly smaller magnitudes for the protruding nozzle case, so the conclusions drawn here are general to both nozzle configurations.

Near the jet exit (at  $x = 0.1rd$ ), the averaged normal stress components  $\langle u'^2 \rangle$  and  $\langle v'^2 \rangle$  show peaks on both the windward and wake sides of the jet. These reflect the dominance of the jet shear layer instability in the near field. The stress component in the jet initial momentum direction,  $\langle u'^2 \rangle$ , has higher magnitude than  $\langle v'^2 \rangle$  in the near field, which was also noted in the LES of Yuan *et al.* (1999); Yuan attributed the reduced  $\langle v'^2 \rangle$  to suppression by strong pressure gradients in the  $y$ -direction. At  $x = 1.0rd$ , approximately the end of the potential core, the roll-up structures in the shear layer have met, giving single peaks in the  $\langle u'^2 \rangle$  and  $\langle v'^2 \rangle$  profiles. The peak values of  $\langle u'^2 \rangle$  and  $\langle v'^2 \rangle$  are then comparable, though the maximum  $\langle u'^2 \rangle$  occurs just to the windward side of the centre streamline, and the maximum  $\langle v'^2 \rangle$  lies to the wake side. This slight misalignment of the maximum  $\langle u'^2 \rangle$  and  $\langle v'^2 \rangle$  persists throughout the measurement region. Yuan *et al.* (1999) found that sufficiently far downstream, the  $\langle u'^2 \rangle$  profile once again takes on a bimodal shape, as turbulence generated by shear between the jet and crossflow fluid produces a local peak in the wake region. This was not observed in the present measurements, which is probably due to insufficient downstream extent of the measurement area.

The turbulent shear stress,  $\langle u'v' \rangle$ , in the near field of the jet takes on high negative values on the windward side, and high positive values on the wake side. These stresses

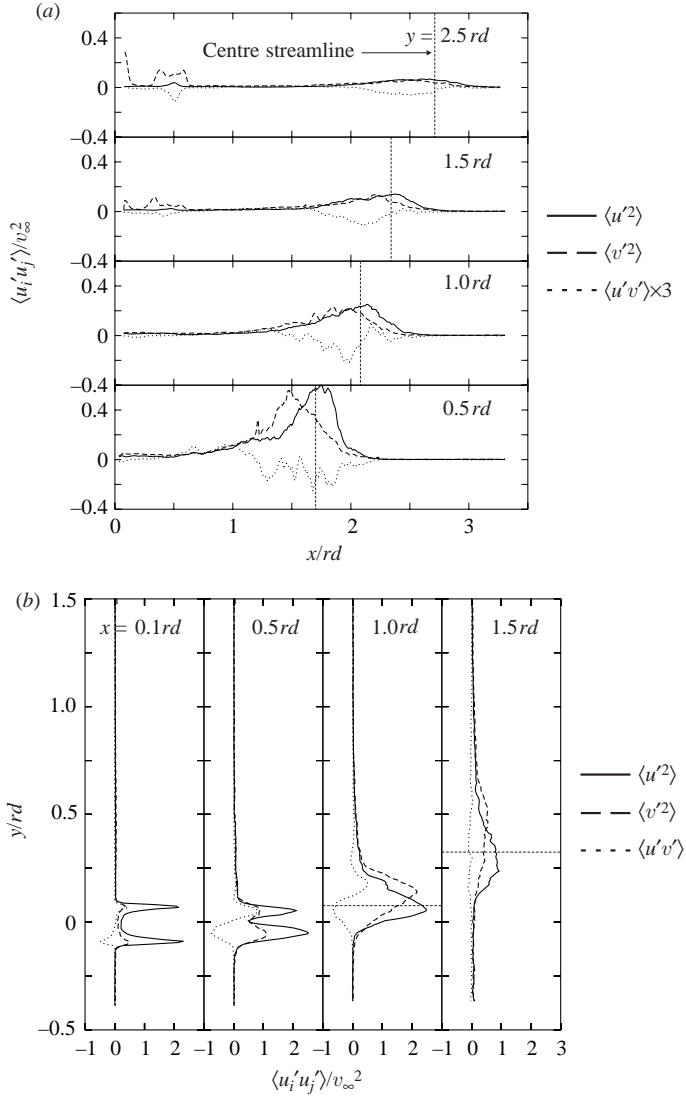


FIGURE 37. Stress profiles in the jet centreplane, for the flush nozzle case. (a) The profiles of  $y = 0.5rd$ ,  $1.0rd$ ,  $1.5rd$  and  $2.5rd$  and (b) the profiles for  $\langle u'^2 \rangle$ ,  $\langle v'^2 \rangle$  and  $\langle u'v' \rangle$  for  $x = 0.1rd$ ,  $0.5rd$ ,  $1.0rd$  and  $1.5rd$ . The fixed- $y$  profiles of  $\langle u'v' \rangle$  in (a) are stretched by a factor of 3.

also result from the jet shear-layer instability. As the flow evolves, the dominant mechanism for generation of  $\langle u'v' \rangle$  becomes shear between the jet and crossflow fluid. At  $y = 1.0rd$ , regions of negative  $\langle u'v' \rangle$  begin to dominate, slightly to the wake side of the centre streamline, with positive values to either side. The regions of positive  $\langle u'v' \rangle$ , particularly that on the windward side, become progressively weaker relative to the regions of negative values for increasing  $y$ . These trends are consistent with those found by Andreopoulos & Rodi (1984) in an  $r = 2$  jet. As the jet bends in the crossflow direction, the sign of  $\langle u'v' \rangle$  generally correlates with the sign of  $-\partial \langle v \rangle / \partial x$ . The deficit velocity due to the wake-like character of the jet is manifested in the positive  $\langle u'v' \rangle$  on the wake side of the jet and negative  $\langle u'v' \rangle$  on the windward side.

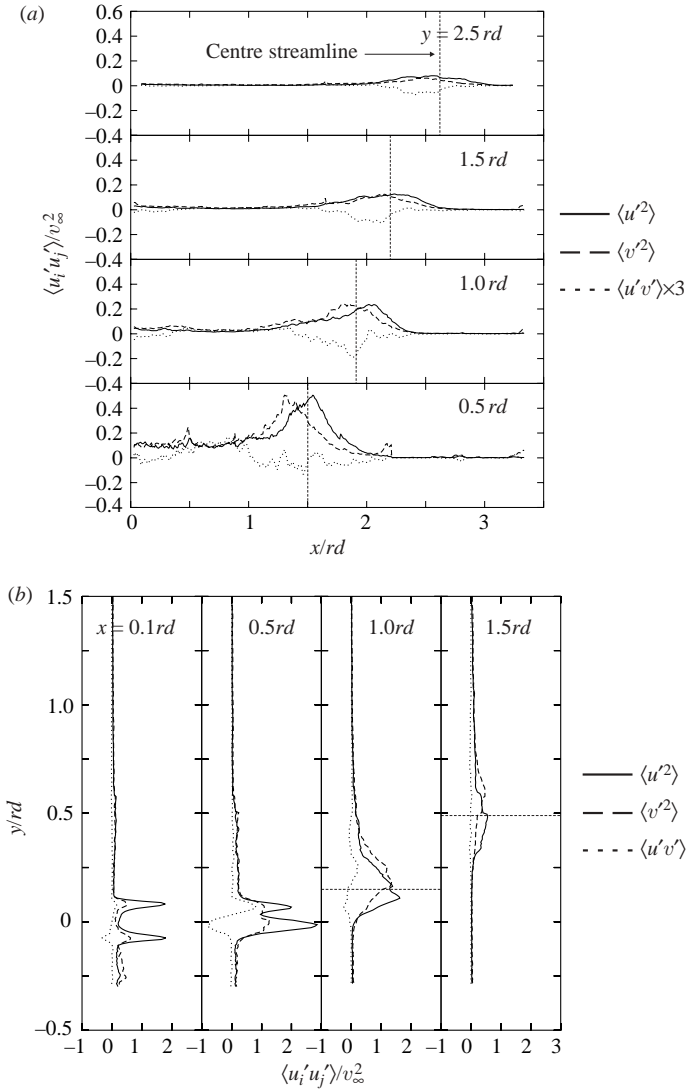


FIGURE 38. Stress profiles in the jet centreplane, for the protruding nozzle case. (a) The profiles of  $\langle u'^2 \rangle$ ,  $\langle v'^2 \rangle$  and  $\langle u'v' \rangle$  for  $y = 0.5rd$ ,  $1.0rd$ ,  $1.5rd$  and  $2.5rd$  and (b) the profiles for  $x = 0.1rd$ ,  $0.5rd$ ,  $1.0rd$  and  $1.5rd$ . The fixed- $y$  profiles of  $\langle u'v' \rangle$  in (a) are stretched by a factor of 3.

The small region of positive  $\langle u'v' \rangle$  on the outer boundary of the jet for small  $y$  arises because as the jet turns, the streamwise velocity on the outer edge exceeds slightly the crossflow velocity.

The turbulent stress profiles in the  $z = 0.22rd$  and  $0.45rd$  planes (figures 39 and 40) largely reproduce the trends from the centreplane, outside the near field. A significant difference between the profiles in the centre and off-centreplanes is that the profile peaks for  $z = 0.22rd$  and  $0.45rd$  are noticeably shifted toward the wake region. The structure of the turbulent stresses thus shows evidence of the characteristic kidney-like structure, depicted in figure 1 and also seen in the scalar fields (§ 3.3), but which was not evident in the velocity magnitude fields (§ 4.4).

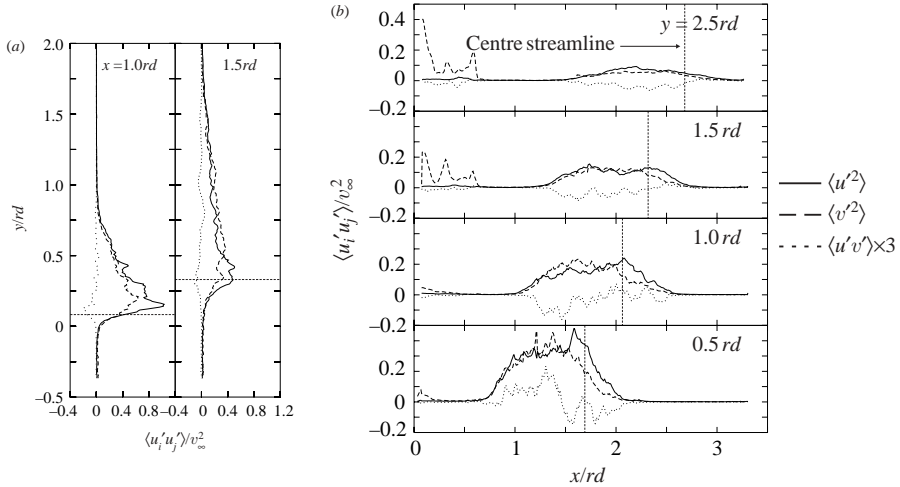


FIGURE 39. Stress profiles in the  $z = 0.22rd$  plane, for the flush nozzle case. (a) The profiles of  $\langle u'^2 \rangle$ ,  $\langle v'^2 \rangle$  and  $\langle u'v' \rangle$  for  $x = 1.0rd$  and  $1.5rd$  and (b) the profiles for  $y = 0.5rd, 1.0rd, 1.5rd$  and  $2.5rd$ . The fixed- $y$  profiles of  $\langle u'v' \rangle$  are stretched by a factor of 3.

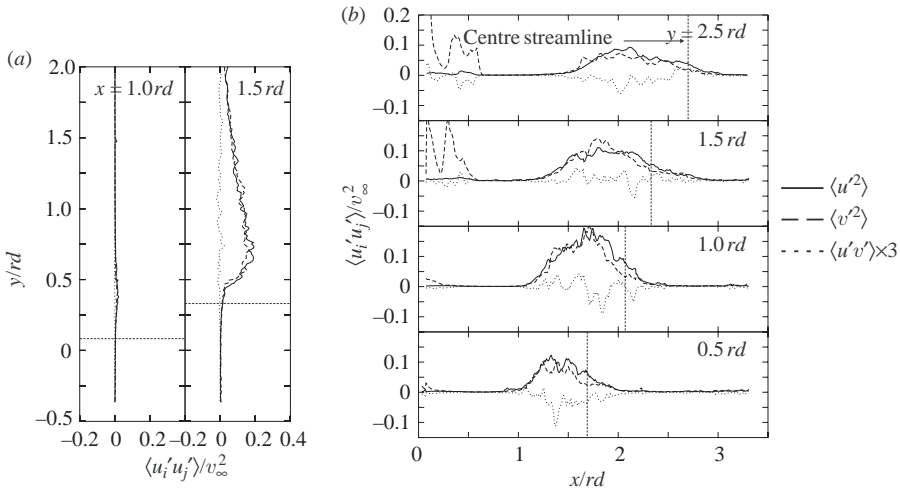


FIGURE 40. Stress profiles in the  $z = 0.45rd$  plane, for the flush nozzle case. (a) The profiles of  $\langle u'^2 \rangle$ ,  $\langle v'^2 \rangle$  and  $\langle u'v' \rangle$  for  $x = 1.0rd$  and  $1.5rd$  and (b) the profiles for  $y = 0.5rd, 1.0rd, 1.5rd$  and  $2.5rd$ . The fixed- $y$  profiles of  $\langle u'v' \rangle$  are stretched by a factor of 3.

## 6. Conclusions

Simultaneous, planar measurements of scalar mixing and two-dimensional velocity fields have permitted the detailed study of the developing region of turbulent crossflowing jets with velocity ratio  $r = 5.7$ . Measurements in off-centreplanes, in addition to the symmetry plane of the flow, give a direct view of the complex three-dimensional nature of the flow.

The scaling properties of the mean flow in the symmetry plane were measured and compared with known scalings for pure jets (in the near field of the crossflowing

jet) and wakes (in the far field). The downstream evolution of the velocity field more closely follows these canonical scalings in the appropriate limits than does the evolution of the scalar field. The scalar centreline value,  $C_m$ , decays with downstream distance in the near field as  $s^{-1}$ , consistent with jet scaling, though the scalar field flow width in the near field does not observe the jet-like linear growth with  $s$ . In the far field,  $C_m$  decays much faster than  $s^{-2/3}$ , the expected wake decay rate, though the flow width seems to approach the  $s^{1/3}$  wake growth rate. The maximum velocity magnitude,  $|\mathbf{u}|_m$ , in the near field decays slightly faster than  $s^{-1}$ . However, in the far field, the crossflow-subtracted maximum velocity magnitude,  $|\mathbf{u} - v_\infty \mathbf{e}_y|_m$ , has a decay rate consistent with  $s^{-2/3}$ , and a growth rate consistent with  $s^{1/3}$ .

The departure from jet scaling for both the scalar and velocity fields in the near field is easily explained by consideration of the flow structure. Cross-stream profiles of scalar concentration and velocity magnitude show that the flow becomes asymmetric very near the nozzle exit, with excess values in the wake region of the flow. In the far field, the scalar field profiles in three dimensions are far from axisymmetric, the expected asymptotic state for a wake-like flow, explaining the failure of the scalar field to observe wake scaling. The good agreement with wake scaling of the velocity field, in contrast, is probably explained by the evidence that the crossflow-subtracted velocity field approaches an axisymmetric cross-sectional form in the far field.

These scaling results were found to be consistent between the two flow geometries studied, one with the jet nozzle exit flush with the wind tunnel wall, and one with the jet nozzle exit protruding into the region of uniform crossflow velocity. However, some of the results for the scalar field evolution differ from those of Smith & Mungal (1998), who considered the flush nozzle geometry for a range of velocity ratios,  $r = 5$  to 25, that encompass the present conditions. Although departing from the results of the present work, the results of Smith & Mungal were self-consistent over the full range of  $r$ . The primary difference is that Smith & Mungal used a top-hat jet exit velocity profile, while the present work used a pipe flow profile. It can be concluded that the jet exit velocity profile is more significant in defining the evolution of the crossflowing jet mixing field than the jet nozzle position or the velocity ratio (within the range of  $r$  considered by Smith & Mungal).

Analysis of turbulence quantities in the scalar and velocity fields is permitted by the high resolution of the measurements. Profiles of the scalar variance, the  $x$ - and  $y$ -components of the turbulent scalar flux, and the in-plane turbulent stresses were presented in the jet centreplane and the  $z = 0.22rd$  and  $0.45rd$  planes. The results show that the intensity of the mixing, as quantified by the scalar variance and the magnitude of the turbulent scalar fluxes, is initially higher on the jet windward side, but eventually becomes higher on the wake side.

The results of this paper, for both the mean and fluctuating quantities, should find particular application in the assessment of simulations of crossflowing jet mixing. The disparate scaling properties of the scalar and velocity fields illustrate the inadequacy of treating the mixing problem as a direct analogue of the flow field. The profiles presented here of the turbulent scalar fluxes, for example, will be of direct use in evaluating the accuracy of scalar mixing models used in simulations.

The support of the Center for Turbulence Research, the National Science Foundation, and the former Gas Research Institute in this work is greatly appreciated. Dr Donghee Han and Mr Raymond M. Mirafior provided valued assistance with the experiments.

## REFERENCES

- ALVAREZ, J., JONES, W. P. & SELOUD, R. 1993 Predictions of momentum and scalar fields in a jet in cross-flow using first and second order turbulence closures. In *AGARD Conf. Proc. Computational and Experimental Assessment of Jets in Cross Flow*, pp. 24–1–24–10.
- ANDREOPOULOS, J. 1983 Heat transfer measurements in a heated jet-pipe flow issuing into a cold cross stream. *Phys. Fluids* **26**, 3201–3210.
- ANDREOPOULOS, J. 1985 On the structure of jets in a crossflow. *J. Fluid Mech.* **157**, 163–197.
- ANDREOPOULOS, J. & RODI, W. 1984 Experimental investigation of jets in a crossflow. *J. Fluid Mech.* **138**, 93–127.
- BIRCH, A. D., BROWN, D. R., FAIRWEATHER, M. & HARGRAVE, G. K. 1989 An experimental study of a turbulent natural gas jet in a cross-flow. *Combust. Sci. Tech.* **66**, 217–232.
- BROADWELL, J. E. & BREIDENTHAL, R. E. 1984 Structure and mixing of a transverse jet in incompressible flow. *J. Fluid Mech.* **148**, 405–412.
- CRABB, D., DURÃO, D. F. G. & WHITELAW, J. H. 1981 A round jet normal to a crossflow. *J. Fluids Engng* **103**, 142–153.
- DURANDO, N. A. 1971 Vortices induced in a jet by a subsonic cross flow. *AIAA J.* **9**, 325–327.
- FRIC, T. F. & ROSHKO, A. 1994 Vortical structure in the wake of a transverse jet. *J. Fluid Mech.* **279**, 1–47.
- HAMA, F. R. 1962 Streaklines in a perturbed shear flow. *Phys. Fluids* **5**, 644–650.
- HASSELBRINK, E. F. 1999 Transverse jets and jet flames: structure, scaling, and effects of heat release. PhD thesis, Stanford University.
- HASSELBRINK, E. F. & MUNGAL, M. G. 1996 An analysis of the time-averaged far-field properties of the transverse jet. *AIAA Paper* 96-0201.
- HASSELBRINK, E. F. & MUNGAL, M. G. 2001a Transverse jets and jet flames. Part 1. Scaling laws for strong transverse jets. *J. Fluid Mech.* **443**, 1–25.
- HASSELBRINK, E. F. & MUNGAL, M. G. 2001b Transverse jets and jet flames. Part 2. Velocity and OH field imaging. *J. Fluid Mech.* **443**, 27–68.
- HAVEN, B. A. & KUROSAKA, M. 1997 Kidney and anti-kidney vortices in crossflow jets. *J. Fluid Mech.* **352**, 27–64.
- KAMOTANI, Y. & GREBER, I. 1972 Experiments on a turbulent jet in a cross flow. *AIAA J.* **10**, 1425–1429.
- KARAGOZIAN, A. R. 1986 An analytical model for the vorticity associated with a transverse jet. *AIAA J.* **24**, 429–436.
- KELSO, R. M., LIM, T. T. & PERRY, A. E. 1996 An experimental study of round jets in cross-flow. *J. Fluid Mech.* **306**, 111–144.
- KELSO, R. M. & SMITS, A. J. 1995 Horseshoe vortex systems resulting from the interaction between a laminar boundary layer and a transverse jet. *Phys. Fluids A* **7**, 153–158.
- MEYER, K. E., ÖZCAN, O. & LARSEN, P. S. 2002 Point and planar LIF for velocity-concentration correlations in a jet in cross flow. In *Laser Techniques for Fluid Mechanics: Selected Papers from the 10th International Symposium, Lisbon, Portugal 10–13 July 2000* (ed. R. J. Adrian, D. F. G. Durão, M. V. Heitor *et al.*), pp. 437–448. Springer.
- NIEDERHAUS, C. E., CHAMPAGNE, F. H. & JACOBS, J. W. 1997 Scalar transport in a swirling transverse jet. *AIAA J.* **11**, 1697–1704.
- PATRICK, M. A. 1967 Experimental investigation of the mixing and penetration of a round turbulent jet injected perpendicularly into a transverse stream. *Trans. Instn Chem. Engrs* **45**, T16–T31.
- PRATTE, B. D. & BAINES, W. D. 1967 Profiles of a round turbulent jet in a cross flow. *J. Hydraul. Div. ASCE* **92**, 53–64.
- RAMSEY, J. W. & GOLDSTEIN, R. J. 1971 Interaction of a heated jet with a deflecting stream. *Trans ASME J. Heat Transfer* **93**, 365–372.
- REID, R. C., PRAUSNITZ, J. M. & POLING, B. E. 1987 *The Properties of Gases and Liquids*, 4th edn. McGraw-Hill.
- RIVERO, A., FERRE, J. A. & GIRALT, F. 2001 Organized motions in a jet in crossflow. *J. Fluid Mech.* **444**, 117–149.
- SCHLÜTER, J. U., ANGELBERGER, C., SCHÖNFELD, T. & POINSOT, T. 1999 LES of jets in crossflow and its application to gas turbine burners. In *Proc. First Intl Symp. on Turbulence and Shear Flow Phenomena*, pp. 71–76. Santa Barbara, CA.

- SCHLÜTER, J. U. & SCHÖNFELD, T. 2000 LES of jets in cross flow and its application to a gas turbine burner. *Flow Turbulence Combust.* **65**, 177–203.
- SHERIF, S. A. & PLETCHER, R. H. 1989 Measurements of the flow and turbulence characteristics of round jets in crossflow. *J. Fluids Engng* **111**, 165–171.
- SHERIF, S. A. & PLETCHER, R. H. 1991 Jet-wake thermal characteristics of heated turbulent jets in crossflow. *J. Thermophys.* **5**, 181–191.
- SMITH, S. H. & MUNGAL, M. G. 1998 Mixing, structure and scaling of the jet in crossflow. *J. Fluid Mech.* **357**, 83–122.
- SU, L. K. & CLEMENS, N. T. 2003 The structure of fine-scale scalar mixing in gas-phase planar turbulent jets. *J. Fluid Mech.* **488**, 1–29.
- YUAN, L. L. 1997 Large eddy simulations of a jet in crossflow. PhD thesis, Stanford University.
- YUAN, L. L., STREET, R. L. & FERZIGER, J. H. 1998 Trajectory and entrainment of a round jet in crossflow. *Phys. Fluids* **10**, 2323–2335.
- YUAN, L. L., STREET, R. L. & FERZIGER, J. H. 1999 Large-eddy simulations of a round jet in crossflow. *J. Fluid Mech.* **379**, 71–104.